Long title

PAN deadenylase ensures proper mitosis under conditions of microtubule stress by regulating spindle integrity and promoting cell survival

Short title

PAN deadenylase is required for mitosis in response to microtubule stress

Authors

Jigyasa Verma[1], Zhengcheng He[2], Joshua A.R. Brown[3], Pamela Dean[1], Barry P. Young[1], Stephane Flibotte[4], LeAnn J. Howe[3], Christopher D. Maxwell[2], Calvin D. Roskelley[1], and Christopher J.R. Loewen[1*]

Author Affiliations

[1] Department of Cellular and Physiological Sciences, Life Sciences Institute, University of British Columbia, Vancouver, Canada, V6T1Z3

[2] Department of Pediatrics, British Columbia Children's Hospital, University of British Columbia, Vancouver, Canada, V6H 0B3

[3] Department of Biochemistry and Molecular Biology, Life Sciences Institute, University of British Columbia, Vancouver, Canada, V6T1Z3

[4] Bioinformatics Facility, Life Sciences Institute, University of British Columbia, Vancouver, Canada, V6T1Z3

[*] Corresponding author: Department of Cellular and Physiological Sciences, Life Sciences Institute, University of British Columbia, Vancouver, Canada, V6T1Z3 cloewen@mail.ubc.ca

Abstract

The Poly(A) Tail Length (PATL) of mRNAs of certain cell-cycle regulatory genes undergo significant trimming during M-phase, however the functional importance is unknown. The Ccr4-Not and PAN complexes account for the majority of cytoplasmic poly(A) deadenylation, however a role in M phase has not been described. We find that under conditions of microtubule stress in yeast, loss of PAN deadenylase activity leads to arrest in M phase, defective spindles, and increased cell death. PAN consists of the catalytic subunit Pan2 and the RNA binding subunit Pan3. Consistent with a role in mitosis, *PAN2* interacts genetically with tubulin genes, prefoldin complex genes and the mitotic cyclin *CLB1*. *PAN2* knockdown in human cultured cells disrupts mitosis and results in spindle fragmentation leading to abnormal cell division, while expression of human *PAN2* in yeast rescues *pan2*Δ cell-cycle phenotypes. Hence, we reveal an important highly conserved role for PAN in ensuring proper mitosis when cells are under microtubule stress. We propose PAN regulates PATLs of mRNAs of key cell-cycle/mitotic proteins in response to defective spindles.

Author Summary

Proper cell division is essential for the growth and survival of all living organisms. Our study investigates the role of PAN deadenylase complex in yeast and human cultured cells under microtubule stress, induced by microtubule inhibitors used in cancer treatment. The PAN complex, consisting of Pan2 and Pan3, trims the poly(A) tails of mRNAs. We found that loss of PAN activity leads to cell cycle arrest in M-phase, spindle defects and increased cell death in yeast. Similarly, *PAN2* knockdown in human cultured cells disrupts mitosis and causes abnormal cell division, indicating a conserved function across species. We propose that PAN regulates mRNA poly(A) tail lengths of key mitotic proteins to ensure proper mitosis under stress. This regulation likely prevents faulty spindle formation by repressing translation of these mRNAs. Interestingly, PAN's role is specific to stress conditions, as cells without PAN function normally otherwise. Our findings highlight PAN's critical role in maintaining genomic stability and proper cell division during microtubule stress, providing insights into the post-transcriptional regulation of cell cycle and potential targets for cancer therapy.

Introduction

In eukaryotes, poly(A) tails are present on the 3' end of almost every mRNA and regulate mRNA stability and translation (1–6). Poly(A) tail length (PATL) varies greatly from as short as ~20 nucleotides to as long as ~250 nucleotides and is governed by poly(A) deadenylases, which trim or remove the tails completely (7–10). Two protein complexes, PAN (PolyA Nuclease) and Ccr4-Not, carry out the majority of deadenylation, where PAN initiates trimming of longer tails while Ccr4-Not removes the remainder (11–14). Poly(A)-Binding Proteins (PABs) bind poly(A) tails promoting deadenylation by recruiting PAN complex to poly(A) tails. Genes such as *CDK1*, *TOP2A* and *FBXO5*, which orchestrate timing and coordination of mitotic events in somatic cells, exhibit reduced PATLs specifically in M-phase (15), suggesting deadenylation of specific mRNAs is important in cell-cycle regulation. However, roles for specific deadenylases in the cell-cycle are poorly defined.

The structure of PAN complex is well understood. It comprises the catalytic subunit Pan2 and an asymmetric homodimer of the RNA-binding regulatory subunit Pan3 (16–18). Pan2 contains a C-terminal DEDD-family exoribonuclease domain that is responsible for its poly-A deadenylase activity. Adjacent to the exoribonuclease domain is a ubiquitin-specific protease (USP) domain, which in human cells is functional (19,20). *Saccharomyces cerevisiae* Pan2 has this domain also, but it lacks critical residues in the catalytic triad indicating yeast Pan2 lacks deubiquitinase activity (16,17). Pan3 contains a CCCH-type zinc finger domain and a Poly(A) interacting motif 2 (PAM2) motif that interacts with PABs facilitating RNA binding. Pan3 also contains a pseudokinase domain (21). Pan2 is a substrate of Cdk1 phosphorylation (22). Pan3

phosphorylation regulates binding to PABs which regulates PAN activity (23), and Pan3 is a substrate of Cdk5 phosphorylation (24,25).

The biological relevance of PANs deadenylase activity is poorly understood. In human cells, knockdown of *PAN2* leads to an increase in mRNAs with long poly(A) tails (> ~150 nt), but does not alter mRNA half lives (14). Deletion of either *PAN2* or *PAN3* in yeast leads to longer mRNA poly(A) tails, but does not completely abolish deadenylation (11,12). This suggests that PAN's role may be more specialized than regulating stability of bulk mRNAs, which has been shown for *HIF1A* regulation (26). In yeast, a protein serine/threonine kinase involved in replication fork protection and the DNA damage checkpoint, Dun1, interacts with Pan2 and Pan3 and regulates the composition and activity of post-replication repair complexes. The *dun1*Δ*pan2*Δ strain is hypersensitive to replication stress and has elevated levels of an important regulator of error-free post-replication repair, Rad5 (27). This suggests PAN plays a role in post-transcriptional regulation of DNA repair and replication stress although the mechanism and mRNA targets are unknown.

We have identified a previously unknown role of PAN complex in cell-cycle regulation. High throughput data indicate that both yeast *PAN2* and *PAN3* exhibit strong aggravating genetic interactions with genes that encode tubulin and tubulin folding proteins (28), and Δ*pan2* and Δ*pan3* yeast are among the most sensitive in the yeast deletion collection to various microtubule biogenesis inhibitors, including nocodazole and benomyl (29). This suggested to us an important, yet uncharacterized function for PAN in mitosis in yeast in response to microtubule stress. We found that nocodazole caused PAN-deficient cells to arrest in M phase, likely due to defective

spindle assembly, resulting in increased cell death. Transcriptional profiling of cells expressing deadenylase-dead Pan2 in the presence of nocodazole revealed changes in key cell-cycle regulators, further supporting a function for PAN in mitosis. We extended our findings from yeast to mammalian cells by knocking down *PAN2* in human cells, which caused spindle fragmentation and defective mitosis upon treatment with nocodazole and colchicine, indicating this function of PAN is conserved in metazoans.

Results

Yeast deletion mutants *pan2*Δ and *pan3*Δ are sensitive to nocodazole

On querying for information on the effects of small molecules on the growth of *pan2*Δ and *pan3*Δ yeast deletion mutants, we noticed that homozygous deletion of *PAN2* or *PAN3* sensitizes yeast to multiple drugs that disrupt tubulin biogenesis (29). These include nocodazole, benomyl, and a number of other small molecules that belong to the response signature 'tubulin folding and SWR complex'. Importantly, both *pan2*Δ and *pan3*Δ are ranked in the top 20 out of over ~4,800 yeast deletion mutants for nocodazole and benomyl sensitivity (29) (**SFig 1A**). Other homozygous deletion strains which occupied top ranks are *pac2*Δ*, cin1*Δ*, cin2*Δ, and *tub3*Δ. *TUB3* encodes α-tubulin, which associates with β-tubulin (*TUB2*) to form tubulin dimers, which polymerize to form microtubules. Pac2 is an alpha tubulin-binding protein, Cin1 is a beta-tubulin-binding protein, and Cin2 is a GTPase activator involved in tubulin complex assembly (30–33). Hence, Pac2, Cin1, and Cin2 are involved in protein folding and assembly of the tubulin complex. This suggested a role for PAN complex in microtubule related functions.

119 Figure S1

S1A

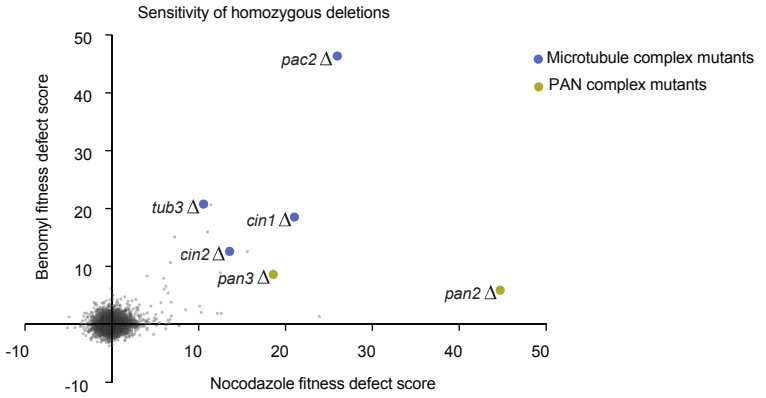

S1B

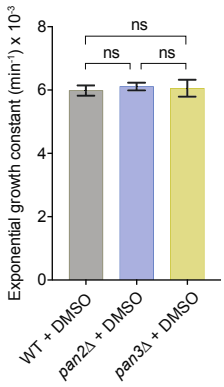

S1C

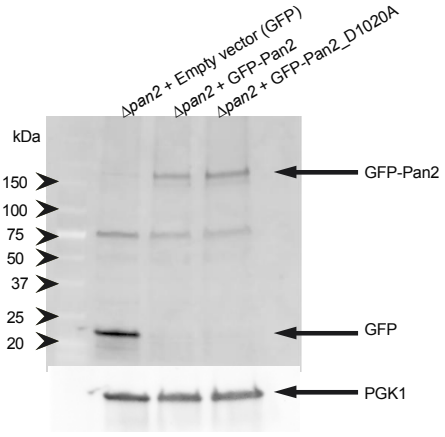

S1D

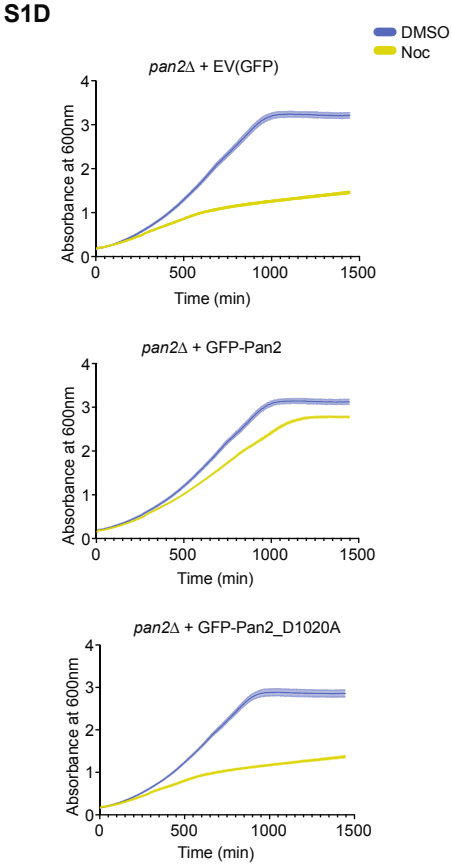

120

Fig S1A: Sensitivity of yeast homozygous deletion strains to nocodazole and benomyl. Ratio of fitness defect scores for over ~4,800 mutants (x-axis: nocodazole; y-axis: benomyl). Blue circles: microtubule complex mutants; green circles: PAN complex mutants. Data from A. Y. Lee et al. 2014. **Fig S1B**: Exponential growth constants for WT, *pan2*Δ, and *pan3*Δ with DMSO. Error bars: +/- SD (n=6, three experiments). Paired Student's *t*-test for strain differences. **Fig S1C**: GFP-Pan2 on plasmid assesses Pan2 expression in D1020A. Upper band: Pan-GFP; lowermost band: free GFP. PGK1 - loading control. CEN, centromeric; GFP, green fluorescent protein. **Fig S1D**: Growth curves of yeast strains with DMSO (blue) or 6 µM nocodazole (yellow) at 30°C for 24 hours. Absorbance plotted with SD (n=6). min, minutes; SC, Synthetic Complete media; SD, standard deviation; EV, empty vector; D1020A, deadenylase dead Pan2.

The nocodazole sensitivity screen described above was performed at 6 µM, while the typical concentration used for inducing G2/M arrest is 40 µM (34). Since the screen produced a phenotype at 6µM (29), we treated log phase cells of *pan2*Δ, *pan3*Δ, and their isogenic wild-type strain with 6 µM nocodazole to mimic the screen and measured yeast growth. While no difference in growth rate was observed for WT, *pan2*Δ and *pan3*Δ grew substantially slower in the presence of nocodazole (**Fig 1A**), but not in the absence of nocodazole (**SFig 1B**). Since growth dynamics were monitored immediately upon the addition of nocodazole, we observed a lag period of approximately 100 minutes (~ 1 1/2 hours) before the effect of the drug was noticeable. For this reason, exponential growth rates were not determined for these experiments.

144 Figure 1

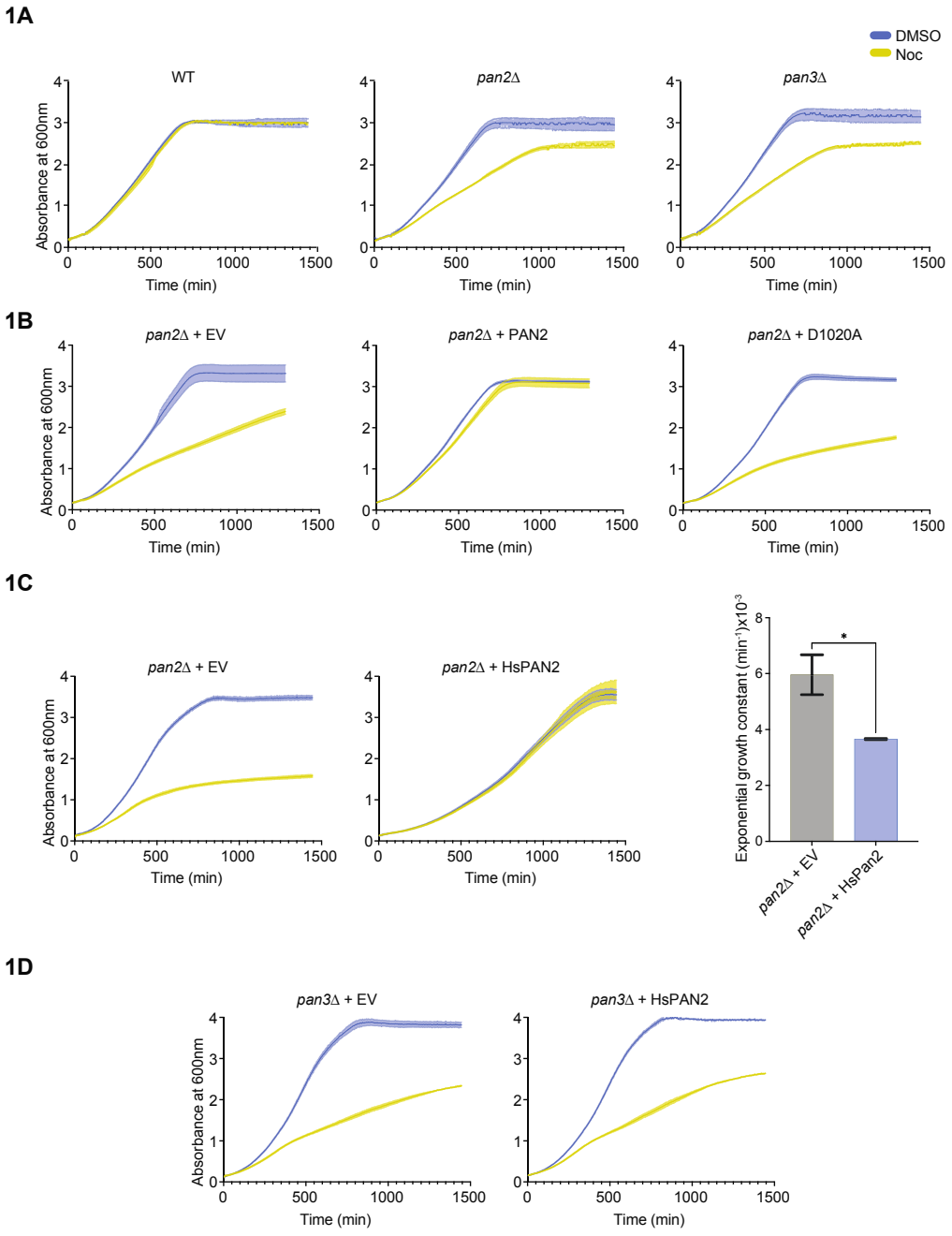

145

Fig 1: Yeast deletion mutants *pan2*Δ and *pan3*Δ are sensitive to nocodazole. (**A-D**) Growth curves of yeast strains in SC media with DMSO (blue) or 6 µM nocodazole (yellow) at 30°C for 24 hours. Absorbance plotted with SD (n=6). Normalized exponential growth constants have been represented in **Fig 1C**. Error bars are +/- SD from three separate experiments (n=6). Significant differences between different strains were tested using paired Student's *t*-test.WT, wild type; min, minutes; SC, Synthetic Complete media; SD, standard deviation; EV, empty vector; D1020A, deadenylase dead Pan2; Hs, *Homo sapiens.*

Expressing WT *PAN2* from a CEN plasmid eliminated the nocodazole sensitivity of *pan2*Δ cells (**Fig 1B**). In contrast, expression of a catalytic-dead mutant of *PAN2* with a mutation within the active site DEDD motif (D1020A) that is unable to perform in-vitro deadenylation on model-polyA RNAs (35) was unable to eliminate the nocodazole sensitivity (**Fig 1B**). To verify that the D1020A mutant was stably expressed, we tagged *PAN2* and the D1020A mutant with GFP and examined protein expression and function. We found no difference in the level of GFP-Pan2 and GFP-Pan2(D1020A) protein (**SFig 1C**). GFP-Pan2 largely eliminated nocodazole sensitivity of *pan2*Δ cells whereas GFP-Pan2(D1020A) did not, confirming that the nocodazole sensitivity is dependent upon Pan2 catalytic activity (**SFig 1D**).

To determine if the role of Pan2 in nocodazole sensitivity is conserved in mammalian cells, we codon-optimized the human *PAN2* gene for expression in yeast (**SFile 1**) and expressed the gene in the *pan2*Δ strain from a high copy 2-micron plasmid (2µ-HsPan2; **Fig 1C**). As was the case with the WT yeast Pan2, expression of HsPAN2 eliminated sensitivity to nocodazole (there was no difference in growth with or without nocodazole in cells expressing HsPan2). Interestingly,

overexpression of HsPAN2 in the *pan2*Δ strain caused a decrease in growth rate (**Fig 1C**). We hypothesized that this reduction in growth would be Pan3 dependent if this phenotype was a result of PAN activity. Indeed, expression of HsPan2 in the *pan3*Δ strain did not not slow growth and did not prevent nocodazole sensitivity (**Fig 1D**). We found a similar slow-growth phenotype with overexpression of yeast Pan2 (see **Fig 5D**). Thus, human Pan2 complemented the function of yeast *pan2*Δ in response to nocodazole, indicating this function of PAN was highly conserved.

***PAN2* and *PAN3* genetically interact with tubulin and genes governing tubulin folding**

To better understand how PAN function was related to nocodazole sensitivity, we examined known common genetic interactions of *PAN2* and *PAN3 (28)* (**SFig 2A**). Gene-ontology (GO) analysis indicated roles for PAN in "chromosome segregation" (*APC1, BUB3, CBF1, MPS1, SLI15, SMC3, TUB2,* and *TUB3*), "cytoskeletal protein binding" (*ARP2, CIN1, GIM3, GIM5, PAC10, RBL2,* and *YKE2*), "secretion" (*ACT1, SEC1, SSO2,* and *VPS27*), and "RNA polymerase-II-specific transcription factor binding" (*CBF1, GCR2,* and *SWI1*) (**SFig 2A**). Within the "chromosome segregation" network, multiple functions relating to microtubules were identified including "spindle", "microtubule cytoskeleton", and "mitotic spindle assembly checkpoint signaling", consistent with a role for PAN in spindle function during mitosis.

188 Figure S2

S2A

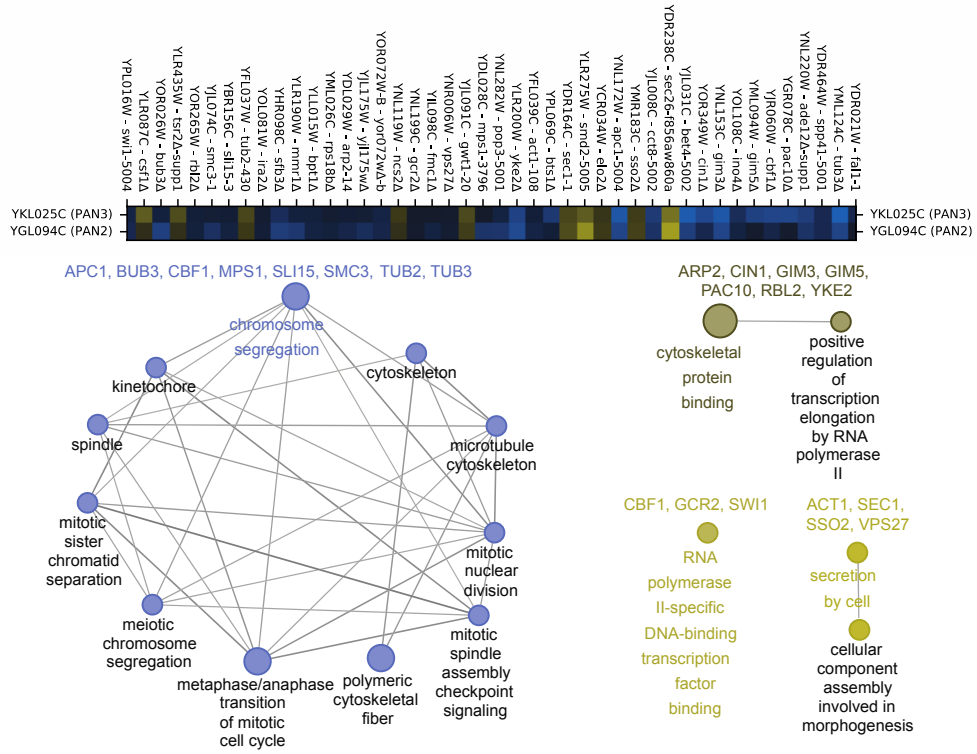

S2B

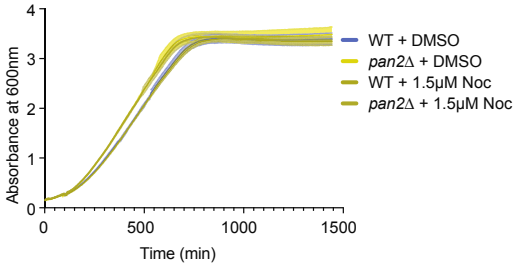

189

S2C

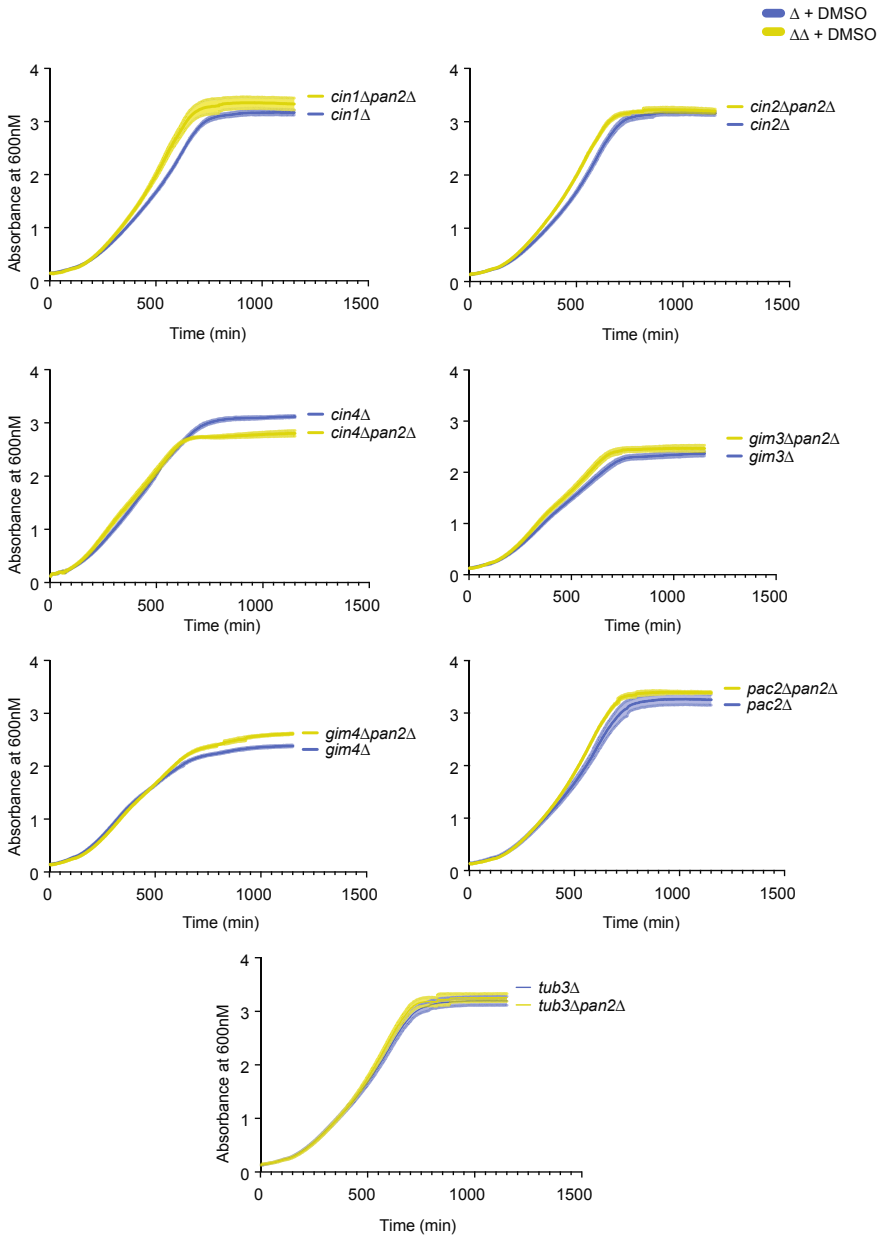

190

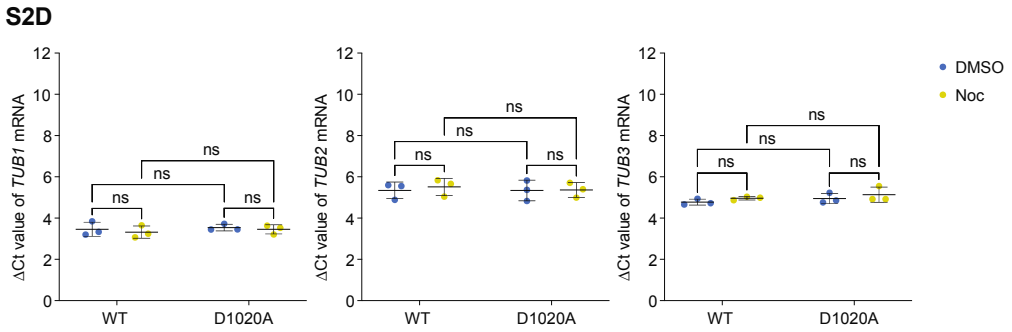

Fig S2A: Heatmap and Cytoscape analysis of genetic interactions of PAN2 and PAN3 by Costanzo et al., 2016. In the heatmap, darker shades of blue represent strong aggravating genetic interactions and darker shades of yellow represent strong alleviating genetic interactions. In the functional enrichment, node size indicates statistical significance of enriched GO terms and edges indicate statistically significant associations between terms. **Fig S2B-C**: Growth curves of yeast strains with DMSO or 1.5 µM nocodazole (B) and single or double knockout strains in DMSO (C). Absorbance plotted with SD (n=6). **Fig S2D**: Gene expression changes in *pan2*Δ+WT-PAN2 or *pan2*Δ+D1020A-PAN2 post 6 hour treatment with DMSO or 6 µM nocodazole assessed by qRT-PCRs. The ΔCt values are normalized to actin. Data are mean +/- S.D. n.s., not significant. Significant differences between all pairwise combinations of groups was detected using two-way ANOVA comparison. Ct, cycle threshold; µM, micromolar; qRT, quantitative reverse transcriptase; ANOVA, Analysis of Variance. min, minutes; SC, Synthetic Complete media; SD, standard deviation; WT, wild type.

206 To validate the genetic interactions described above and expand the interaction landscape to
207 include microtubule stress from nocodazole treatment, we performed synthetic genetic array
208 (SGA) double mutant screens with a *pan2*Δ query and the non-essential deletion collection of
209 ~4800 strains in the absence and presence of nocodazole (1.5μM nocodazole as this does not
210 lead to differential growth between WT and *pan2*Δ in liquid growth assays, **SFig 2B**). In the
211 absence of nocodazole using a cut-off ratio of 0.7 for aggravating genetic interactions (three
212 standard deviations, 99.7% confidence interval) and p-value of less than 0.05 in 3/3 replicates,
213 we found a total of 52 genetic interactions. For deletion mutants in the array whose growth was
214 rescued upon deleting *PAN2* in them (referred to as alleviating genetic interactions from here
215 onwards), we chose a cut-off ratio of 1.3 and found 27 genetic interactors (**SFile 2**). The 4 genes
216 in common with the previously identified genetic interactors (28) were *TUB3, BUB3, RPL12B,*
217 and *RPL14A*. Surprisingly, all the genes with functions related to chromosome segregation were
218 not identified in the absence of nocodazole, but instead required addition of low levels of
219 nocodazole (see below).
220
221 For SGA screens in the presence of nocodazole, we used a low nocodazole concentration (1.5
222 μM) anticipating that the genetic interactors themselves might be nocodazole sensitive, and that
223 this dose would not produce a growth phenotype in the *pan2*Δ query strain (**SFig 2B**). Using the
224 same cut-offs as the no-nocodazole screens, we identified a total of 30 aggravating and 21
225 alleviating genetic interactions (**SFile 2**). Of these, 7 genetic interactors were in common with
226 the PAN interactions from the CellMap (**Fig 2A**). These genes were *CIN1, GIM3, MDM32,*
227 *PAC2, TUB3, VPS68* and *YKE2*. *CIN1, GIM3, PAC2,* and *YKE2* are involved in tubulin folding
228 and tubulin complex assembly. *CIN1* encodes for tubulin folding factor D involved in beta-

229 tubulin (Tub2) folding (36). *GIM3*, *PAC2,* and *YKE2* encode for subunits of the prefoldin co-
230 chaperone complex involved in tubulin folding (37). *TUB3* encodes alpha-tubulin which
231 associates with beta-tubulin (Tub2) to form the tubulin dimer. It is unclear why nocodazole was
232 required to detect genetic interactions with microtubule related components in our screens, but
233 not those performed by the Boone lab (28) however, screen conditions (query strain background,
234 media composition, temperature, array density) varied between our labs, suggesting perhaps that
235 our screens had reduced microtubule stress, which prevented identification of the interactions, or
236 that their screens had increased stress mimicking nocodazole addition.
237

238 Figure 2

2A

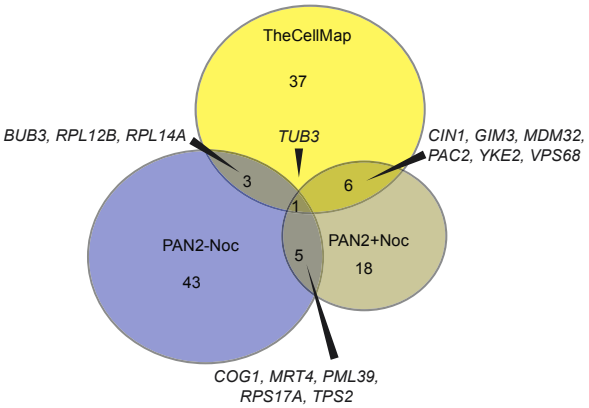

2B

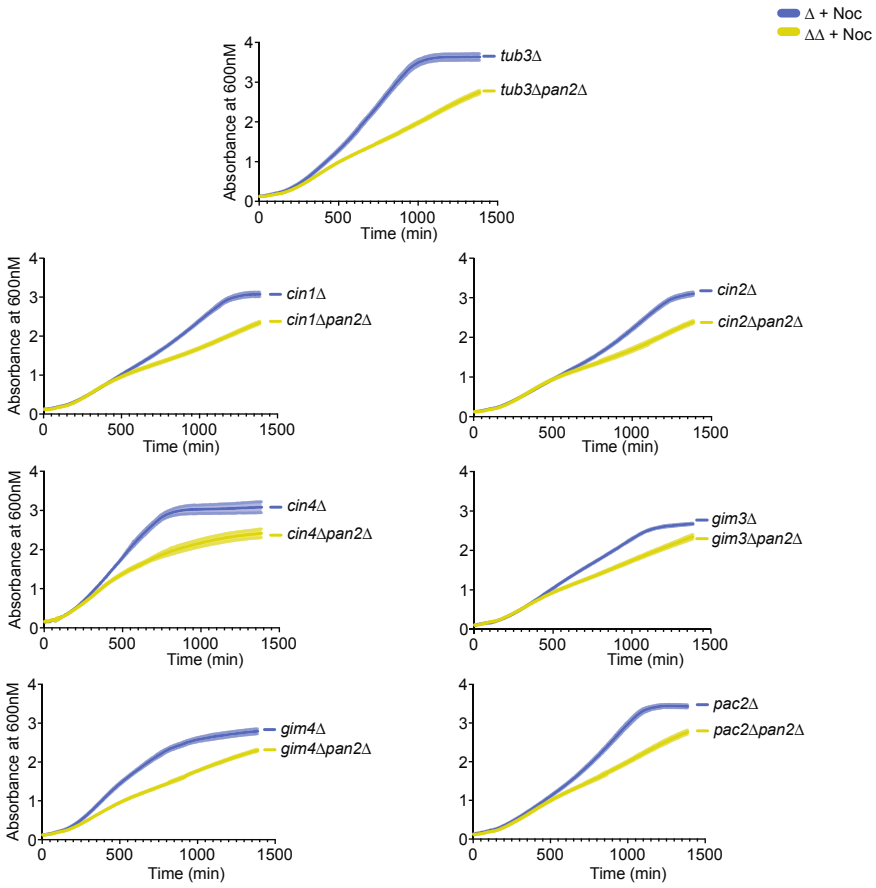

239

Fig 2: PAN2 and PAN3 genetically interact with tubulin and genes governing tubulin folding. (**A**) Venn diagram shows overlap between aggravating genetic interactions for PAN2 according to TheCellMap (yellow), PAN2 SGA screen in either absence (blue) or presence of nocodazole (light brown). **(B)** Growth curves of single knockout (blue) or double knockout (yellow) yeast strains in SC media with 1.5 μM nocodazole for 24 hours at 30°C. Absorbance plotted with SD (n=6). min, minutes; SC, Synthetic Complete media; SD, standard deviation.

To confirm genetic interactions of *PAN2* with genes involved in microtubule function, we assessed the sensitivities of single and double knock-out strains in liquid growth assays using the same low dose of nocodazole used in our screens (1.5 μM), which did not affect the growth of *pan2*Δ single mutant cells (**SFig 2B**). We confirmed slow growth phenotypes in double mutants with *CIN1, GIM3, PAC2,* and *TUB3* in the presence of 1.5 μM nocodazole (**Fig 2B**), indicating aggravating genetic interactions with these genes. There was no difference in growth of the single and double knockouts in the absence of drug (**SFig 2C**), consistent with our screen results. We also expanded our test set to include other genes involved in tubulin folding including *CIN2* (GTPase activating protein, tubulin folding cofactor C), *CIN4* (GTPase involved in beta-tubulin folding, regulated by *CIN2*), and *GIM4* (prefoldin co-chaperone complex). These all showed aggravating genetic interactions with *PAN2* in the presence of 1.5 μM nocodazole but not in the absence. Since PAN regulates mRNA stability, we were intrigued to test the mRNA levels of tubulin genes *TUB1, TUB2,* and *TUB3*, in the presence and absence of nocodazole, but found no significant changes in transcript abundance (**SFig 2D**). Thus, the genetic interactions between *PAN2* and *PAN3* and genes governing tubulin folding provided strong genetic evidence for a role for PAN in microtubule function.

PAN2 deletion exacerbates nocodazole-induced G2/M arrest

Upon establishing the nocodazole sensitivity of *pan2*Δ and *pan3*Δ and genetic interactions between *PAN2* and *PAN3* and genes governing tubulin folding in yeast, we were interested in understanding this phenotype further. We performed flow cytometry to determine the distribution of cells in G1/S and G2/M phases. Log phase cells of *pan2*Δ and WT were treated with either DMSO or 6 µM nocodazole and collected at different time points after treatment (3, 6 and 10 hours). They were fixed in ethanol and stained to analyze DNA content by flow cytometer. In the absence of drug treatment, we saw that both *pan2*Δ and WT cells have typical distributions for asynchronous log phase yeast cultures of 1N and 2N cells at all the time points, suggesting normal cell-cycle progression (**Fig 3A**). However, upon treatment with nocodazole, we found that there was a shift from 1N to 2N and a broadening of the 2N peak in *pan2*Δ as compared to WT cells at 3 hours, indicating a G2/M delay (**Fig 3A**). We did not observe a discrete 1N peak and the DNA content extended beyond 2N, suggesting genomic instability or an extensive G2/M arrest in *pan2*Δ cells after 6 hours of treatment with nocodazole (and also at 10 hours) (**Fig 3A**).

279 Figure 3

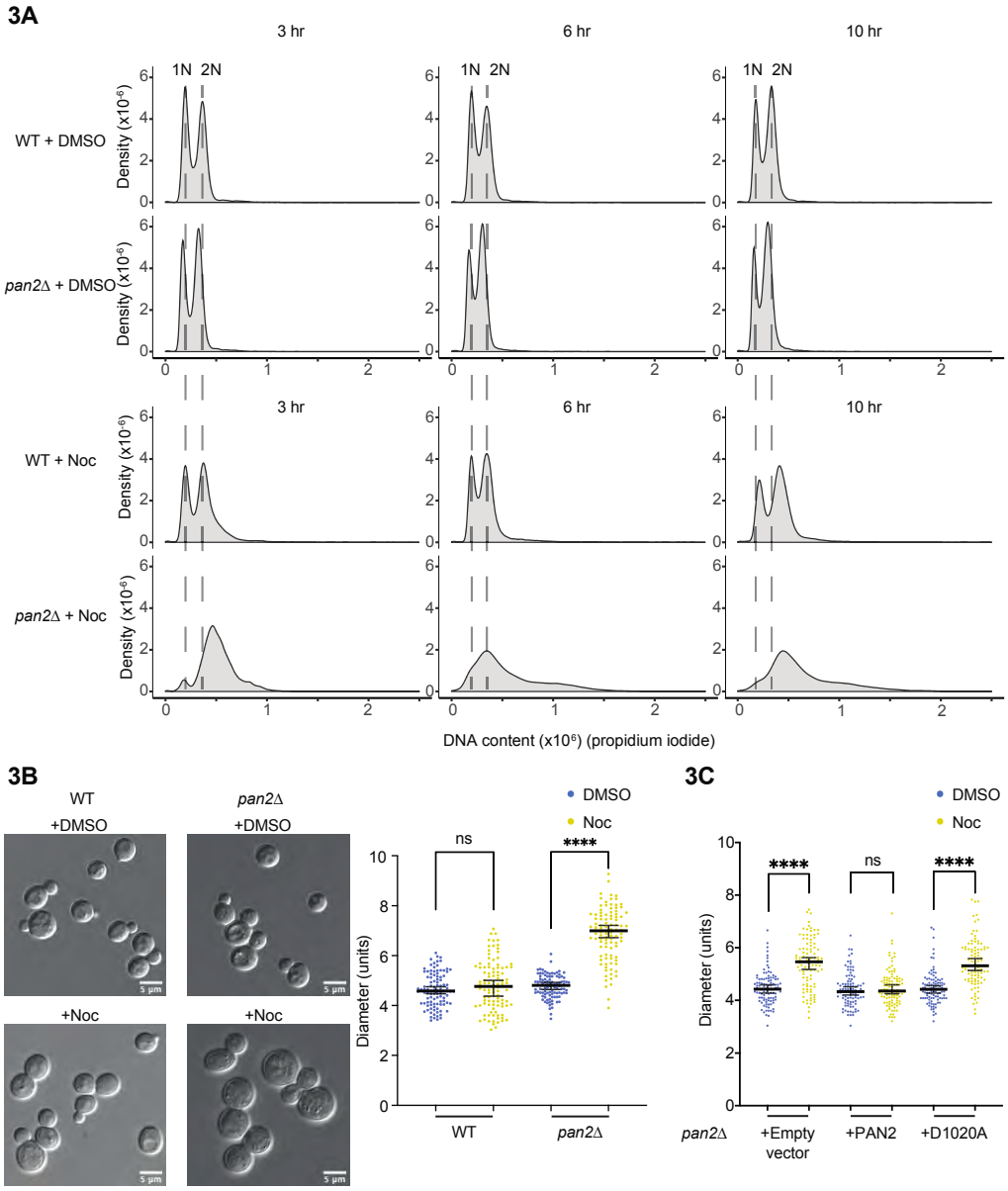

280

Fig 3: G2/M delay in *pan2*Δ cells treated with nocodazole. (A) FACS profiles post treatment with DMSO or 6 µM nocodazole. 1N and 2N respectively represent DNA content. Green lines represent the position of 1N and 2N DNA peaks in untreated cells. FACS, fluorescence activated cell sorting; hr, hours; WT, wild type; Noc, nocodazole. **(B-C)** Live imaging of yeast cells treated for 6 hours. Mother cell size quantified (n > 100). Scale bars: 5 µm. Paired Student's t-test for significant differences. WT, wild type; ns, not significant, ****, p<0.0001.

Analysis of the gates during flow cytometry revealed that *pan2*Δ cells upon 3 hours of treatment with nocodazole, had a different forward scatter than WT cells, suggesting that *pan2*Δ cells upon treatment with nocodazole for 3 hours were larger than WT cells (**SFig 3A**), while there was no difference in cell-size upon DMSO treatment (**SFig 3A**). This trend was consistent for the next two time-points as well (6 and 10 hours post treatment with nocodazole), so we determined the cell morphology of *pan2*Δ upon treatment with nocodazole. On treatment of log phase cells with 6 µM nocodazole for 6 hours, *pan2*Δ exhibited a significant increase in cell diameter (~1.75 times), relative to the WT cells, while there was no significant difference in size upon treatment with DMSO (**Fig 3B**). *pan2*Δ cells treated with nocodazole were predominantly large-budded, and together with their increased cell size, were consistent with our FACS data indicating a G2/M delay. Upon expression of WT *PAN2* in *pan2*Δ cells, we were able to eliminate the large cell phenotype, whereas expression of deadenylase-dead *PAN2* did not, indicating the deadenylase activity of Pan2 was required to prevent the G2/M delay (**Fig 3C**).

302 Figure S3

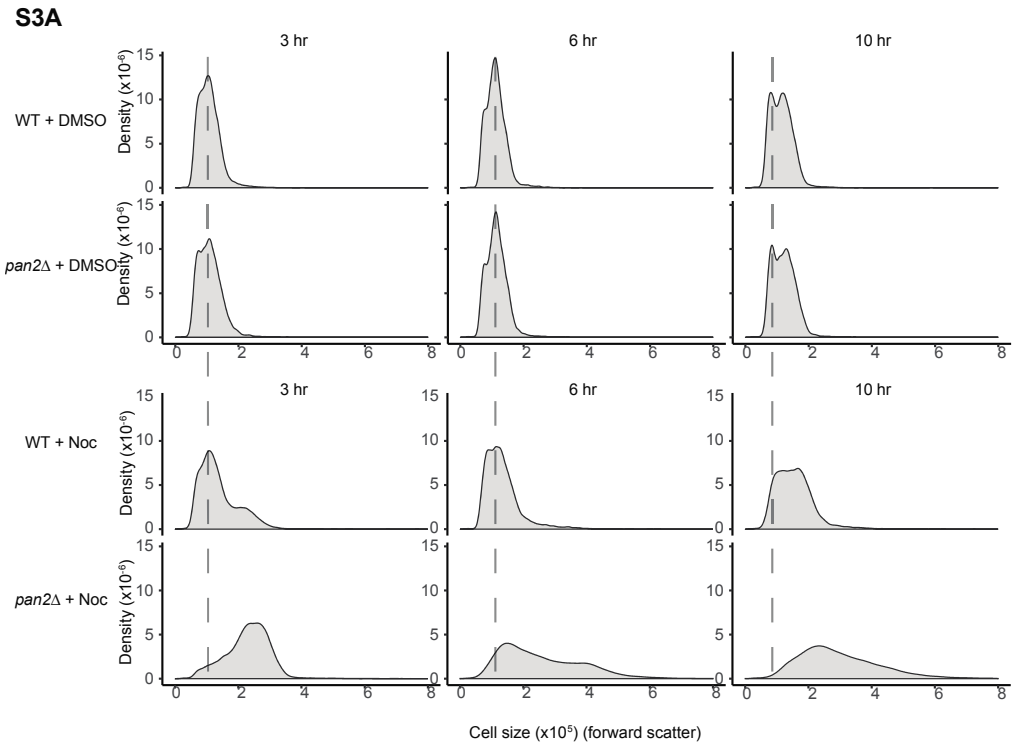

303

304 **Fig S3A**: FACS profiles post DMSO or 6 µM nocodazole treatment. FACS, fluorescence

305 activated cell sorting; hr, hours; WT, wild type.

306

307 **Nocodazole treatment leads to increased cell-death in *pan2*Δ cells due to impaired spindle**

308 **formation**

309

310 We were intrigued to determine if there was a difference in spindle morphology in *pan2*Δ cells

311 upon nocodazole treatment. Thus, we used (Tub1+3'UTR)-yomWasabi cassette (38) to first tag

tubulin. Upon testing the sensitivity of *pan2*Δ-(Tub1+3'UTR)-yomWasabi yeast and WT-(Tub1+3'UTR)-yomWasabi yeast, similar to *pan2*Δ yeast, we found that *pan2*Δ-(Tub1+3'UTR)-yomWasabi yeast was sensitive to nocodazole, and that WT-(Tub1+3'UTR)-yomWasabi yeast exhibited a mild slow-growth phenotype compared to WT (**SFig 4A**). We set up an assay to observe spindle morphology as well as measure the total number of cells, dead cells and cell area using live-cell imaging of yeast and analyzing the data using a machine-learning assisted pipeline (see Methods). In untreated cells, cell growth appeared to be normal and we did not observe significant differences in cell number or number of dead cells in WT vs *pan2*Δ cells over 8 h of imaging (**Fig 4A, left panels; also see movies in SFiles 4 and 6**). Cell area was largely unchanged in both WT and *pan2*Δ cells over the time-course (**Fig. 4B**). Treatment with 6μM nocodazole did not result in a significant difference in total cells or dead cells between WT and Δ*pan2* cells, and cell area remained largely unchanged (**SFig 4B-4C**). This was different from what we observed in liquid growth assay and we suspect was due to the different growth conditions during live-cell imaging (no shaking or aeration), which altered the level of effective drug exposure. Hence, we tested increased drug concentrations. At 12 μM nocodazole we observed a general slowing of growth and a significant difference in total cells ($p<0.0001$) and dead cells ($p<0.0001$) between WT and *pan2*Δ. For WT treated with nocodazole, the mean total cell number was 120 at t=0 and 344.5 at t=480 minutes, while the mean number of dead cells increased from 0.75 to 19.75 (**Fig 4A, top right panel; also see movie SFile 5**), whereas for *pan2*Δ treated with nocodazole the mean total cell number was 125 at t=0 and 199 at t=480 min and the mean number of dead cells increased from 0.25 to 27.75 (**Fig 4A, bottom right panel; also see movie SFile 7**). We also observed a steady increase in cell area of both WT and *pan2*Δ until ~360 min, which then leveled off (**Fig 4B**). This increase in cell area was much greater for

335 *pan2*Δ (~13 µm^2 to ~23 µm^2) than for WT (~12 µm^2 to ~17 µm^2) (**Fig 4B**). Taken together the
336 decreased cell growth, increased cell death and increased cell area of *pan2*Δ cells treated with
337 nocodazole were consistent with these cells having a defective cell-cycle.
338
339 Figure S4

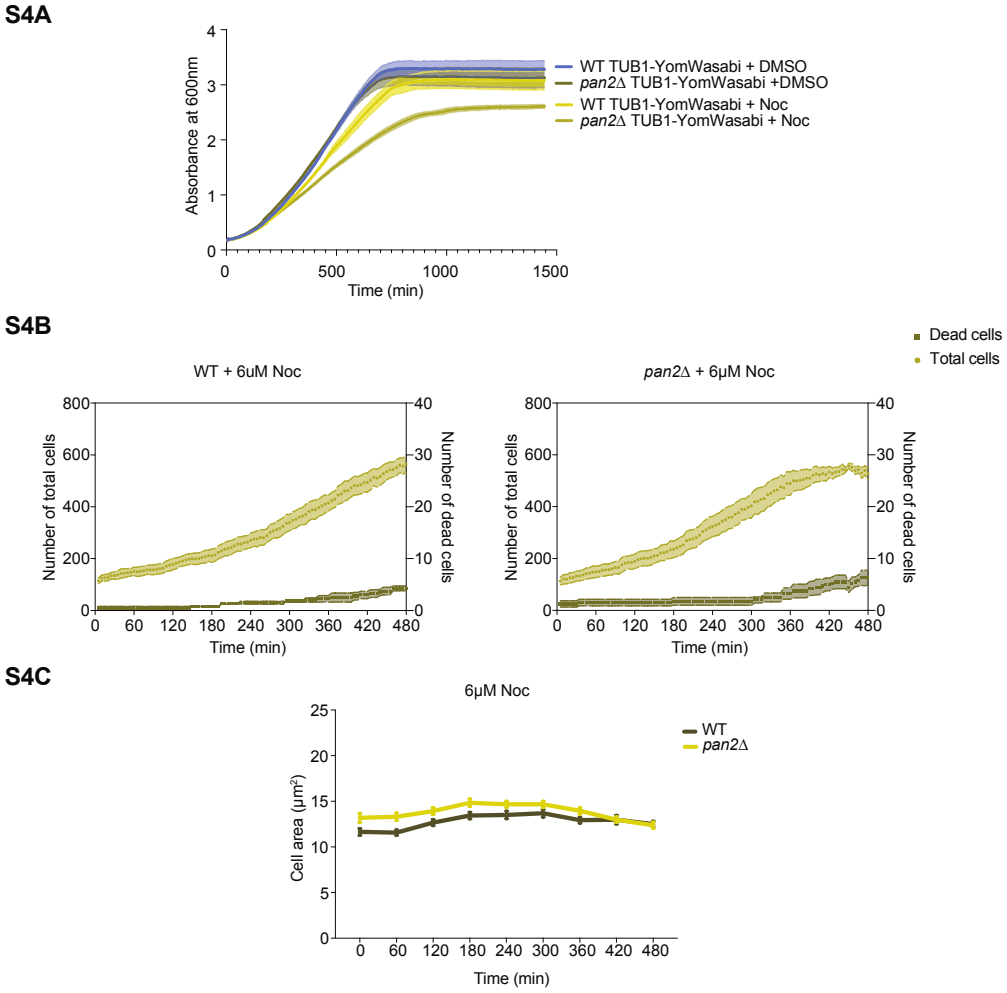

340
341 **Fig S4A**: *pan2*Δ Tub1-yW yeast is sensitive to nocodazole and WT-Tub1-yW exhibits a mild
342 slow-growth phenotype compared to WT. Growth curves of yeast strains grown in liquid SC

media with or without 6 µM nocodazole and monitored for 24 hours. An average of 6 replicates has been plotted with SD. Absorbance adjusted for baseline correction. µM, micromolar; SC, Synthetic Complete media; SD, standard deviation. **Fig S4B:** Number of total cells (left y-axis) and number of dead cells (right y-axis) upon treatment of WT (top) or *pan2*Δ (below) with 6µM nocodazole for every 5-minutes over a total time interval of 480 minutes. **Fig S4C:** Cell area of individual cells of WT (brown) or *pan2*Δ (yellow) is represented with 95% confidence interval upon treatment with 6µM nocodazole over a total duration of 480 minutes. Each time point represents the cell area of 500-2500 cells recognised by cell segmentation.

352 Figure 4

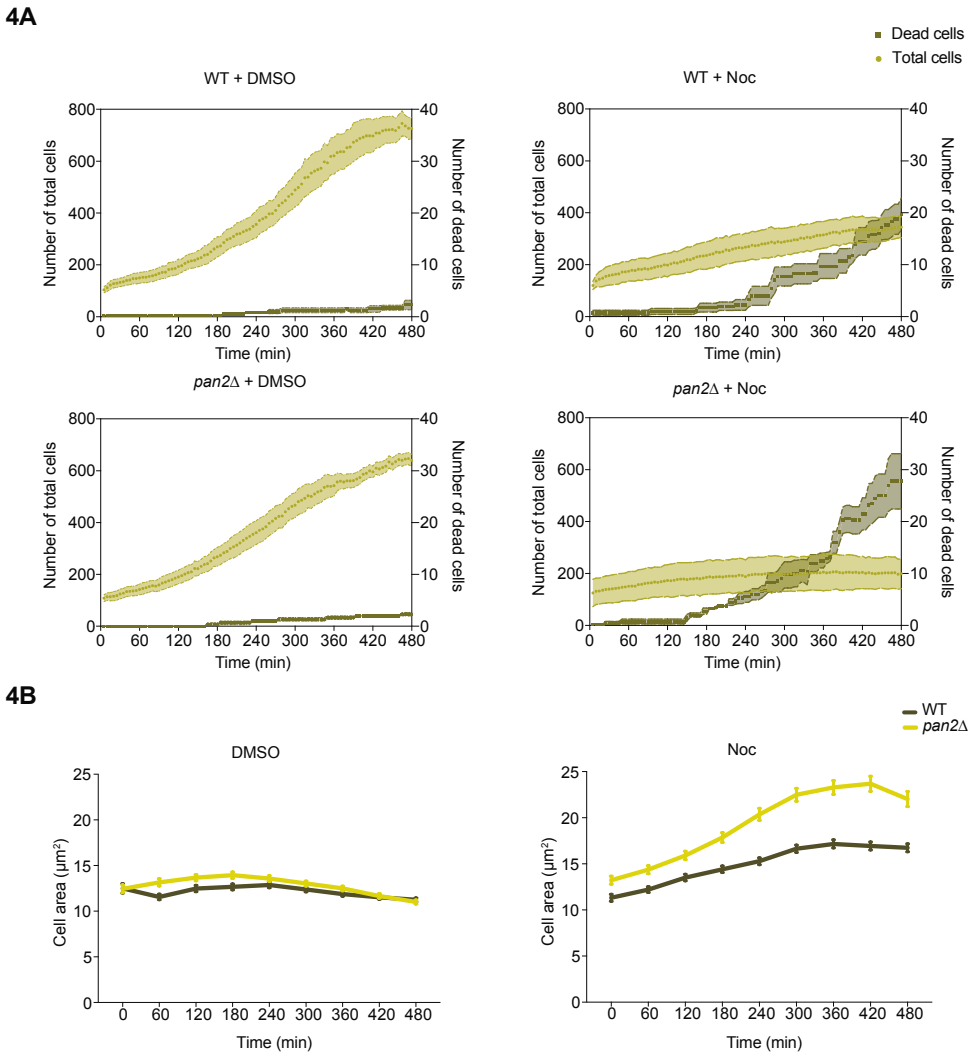

353

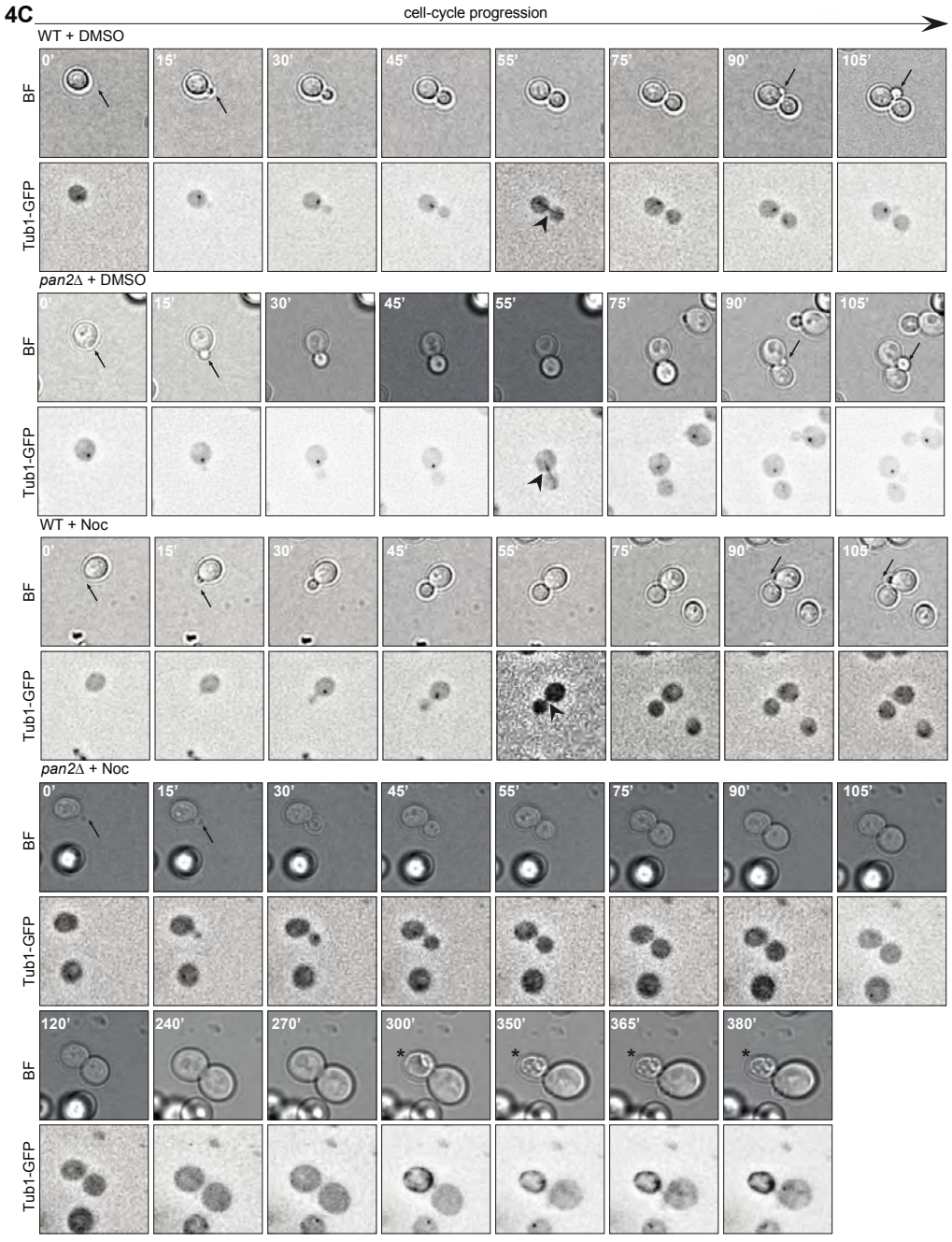

354

355 **Fig 4**: **Spindle defects in *pan2*Δ upon treatment with nocodazole. (A)** Number of total cells

356 (left y-axis) and number of dead cells (right y-axis) upon treatment of WT or *pan2*Δ with DMSO

(left) or 12µM nocodazole (right) for every 5-minutes over a total time interval of 480 minutes were calculated using machine-learning assisted pipelines. **(B)** Cell area of individual cells of WT (brown) or *pan2*Δ (yellow) is represented with 95% confidence interval upon treatment with DMSO (left) or 12µM nocodazole (right) over a total duration of 480 minutes. Each time point represents the cell area of 500-2500 cells recognised by cell segmentation. **(C)** Live imaging of log phase yeast cells expressing (Tub1+3'UTR)-yom-Wasabi WT or *pan2*Δ. The cells are treated with DMSO or 12 µM nocodazole for ~75 minutes prior to imaging. The time-stamps are indicated on top left of each snapshot. Arrow indicates new bud, arrowhead indicates mitotic spindle and asterisk indicates dead cell. WT, wild-type; DMSO, dimethyl sulfoxide; µM, microMolar; Tub1: alpha-tubulin; UTR, untranslated region.

Now next we examined cell morphology and tubulin-tagged spindles in detail. In untreated WT and *pan2*Δ cells, budding and cell division appeared normal with a cell-cycle duration of ~75 min (**Fig 4C**). Spindles appeared normal, with the spindle pole body being clearly visible at the time of bud emergence (15 min, S phase) and then migrating to the bud neck (30 min, G2 phase) before elongating through the neck and into the bud (55 min, M phase). For nocodazole treated cells, we chose to examine cells after 75 min of treatment with 12µM nocodazole because this time corresponded to approximately one round of cell division and there was little cell death at this time point. The WT cell shown had an elongated cell-cycle of ~90 min (compared to ~75 min for untreated cells), however cell morphology and spindles appeared normal (**Fig 4C**; times indicated are relative to the start of the cell-cycle for the given cell). This was consistent with our quantification, which indicated that over this time period cell number increased, there were few dead cells, and there was only a marginal increase in cell size. In contrast, the *pan2*Δ cell shown

did not have clearly detectable spindle pole bodies or spindles, and although bud growth progressed normally for ~90 min, cell division failed to complete and there was continued mother and bud growth leading to very large cells (see 270 min). For this cell, at 300 min the mother died and the now orphan "daughter" failed to grow or divide (as late as 380 min). This was consistent with our quantification, which indicated that cell number did not increase substantially after nocodazole addition, that the number of dead cells increased and there was a substantial increase in cell size. Thus, in *pan2*Δ cells treated with nocodazole, the spindle was compromised which led to defective mitosis and a failure to complete the cell-cycle.

_pan2_Δ cells exhibit dysregulated cell-cycle gene expression in response to nocodazole

Because deadenylase dead PAN2 did not eliminate the nocodazole sensitivity of *pan2*Δ cells, we were interested in the transcriptional profile of these cells and if there were altered expression of cell-cycle genes. Therefore, we performed an RNA-sequencing experiment on nocodazole-treated populations of *pan2*Δ + WT Pan2 and *pan2*Δ + D1020A Pan2 cells to identify differences in the transcriptome. Log phase cultures of the above genotypes in duplicate were treated with 6 µM of nocodazole for 6 hours and mRNA was collected and sequenced. Spearman correlations for expression of all the genes were plotted for the two replicates of the two samples (**SFig 5A**).

399 Figure S5

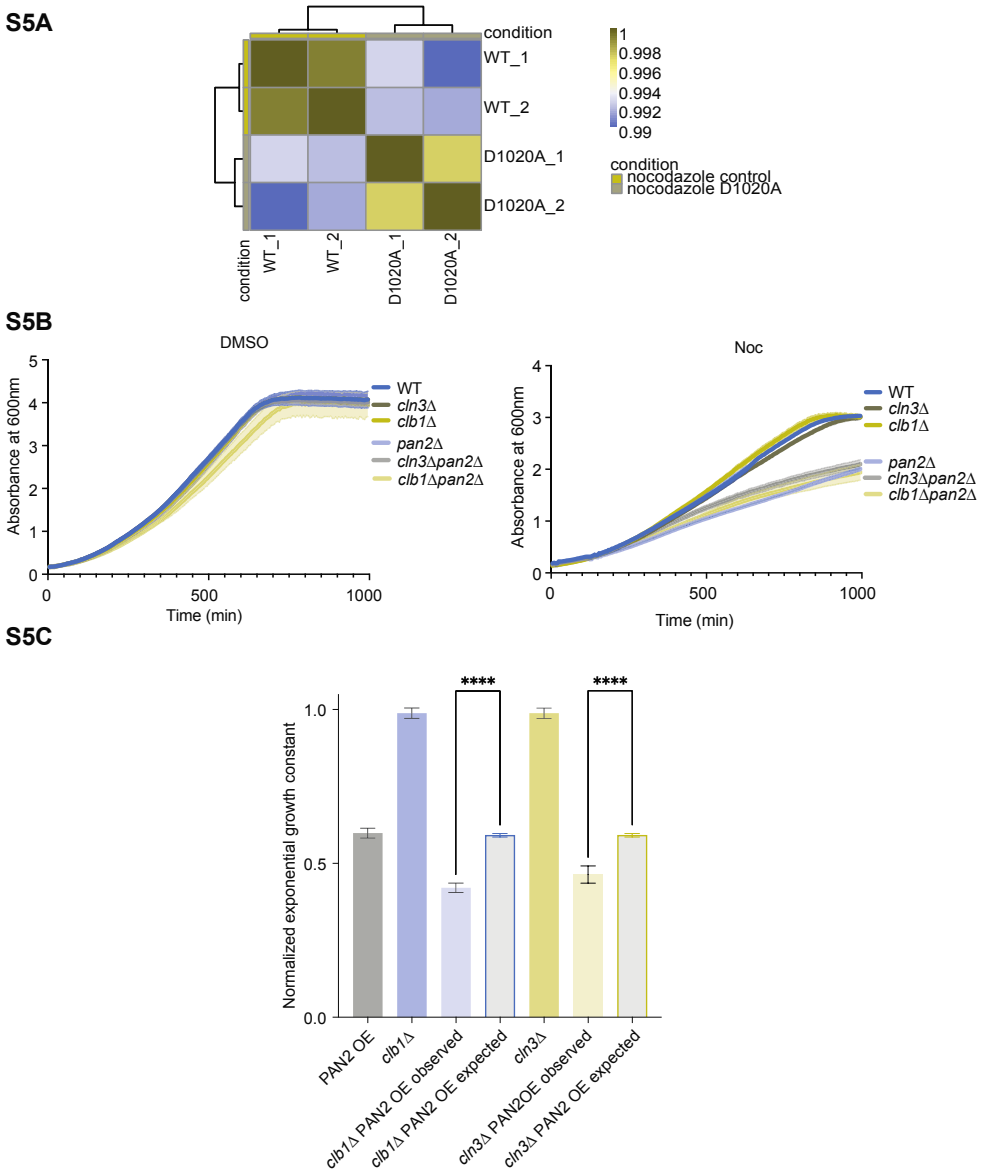

400

Fig S5A: Spearman correlations for expression of all the genes were plotted for the two replicates per sample of nocodazole treated Control and D1020A samples. **Fig S5B**: Growth curves of yeast strains in SC media with DMSO (left) or 6 µM nocodazole (right) at 30°C for 24 hours. Absorbance plotted with SD (n=6). min, minutes; SC, Synthetic Complete media; SD, standard deviation; WT, wild type. **Fig S5C**: Normalized exponential growth constants (data from **Fig 5D**). Error bars are +/- SD from three separate experiments (n=6). Significant differences between different strains were tested using paired Student's *t*-test. OE, overexpression.

Out of the 6,031 ORFs analyzed, we chose an absolute z-score cutoff of 2 (equivalent to a log2 fold change cutoff of 1.182 and -1.0554). For a p value < 0.01 and log2 CPM > 1 (counts per million), we identified 129 upregulated and 39 downregulated genes (**Fig 5A**) (**SFile 3**). These genes were enriched in GO terms related to replication fork protection complex, arginine biosynthetic process, carboxylic acid metabolic process, ascospore wall assembly, thiamine biosynthetic process, hexitol metabolic process and glyoxalase III activity (**Fig 5B**). These processes are known to be cell-cycle dependent and regulated at the transcriptional level, with histone mRNAs (replication fork complex genes) being synthesized exclusively in S phase (39). Hence, the change we see in the expression of these genes was consistent transcriptionally with nocodazole-treated PAN-deficient cells having a G2/M arrest. The transcriptional upregulation of hexitol metabolic process and glyoxalase III activity in *pan2*Δ + D1020A Pan2 compared to *pan2*Δ + WT Pan2, indicates that the cells are likely undergoing a metabolic shift and producing energy differently (hexitol metabolism) and are responding to the oxidative stress in the environment (glyoxalase III activity). While ascospore wall assembly and thiamine biosynthetic

424 processes were also found to be upregulated, since these are haploid cells, it is likely that
425 upregulation of ascospore wall assembly mRNAs is consistent with increased demand for cell
426 wall synthesis during bud growth in G2/M and the increased cell-size of PAN-deficient cells.
427 Some of the genes involved in sporulation might have alternative functions in conditions of
428 nutrient limitation, environmental stress or even mutations that disrupt normal cell-cycle.
429

430 Figure 5

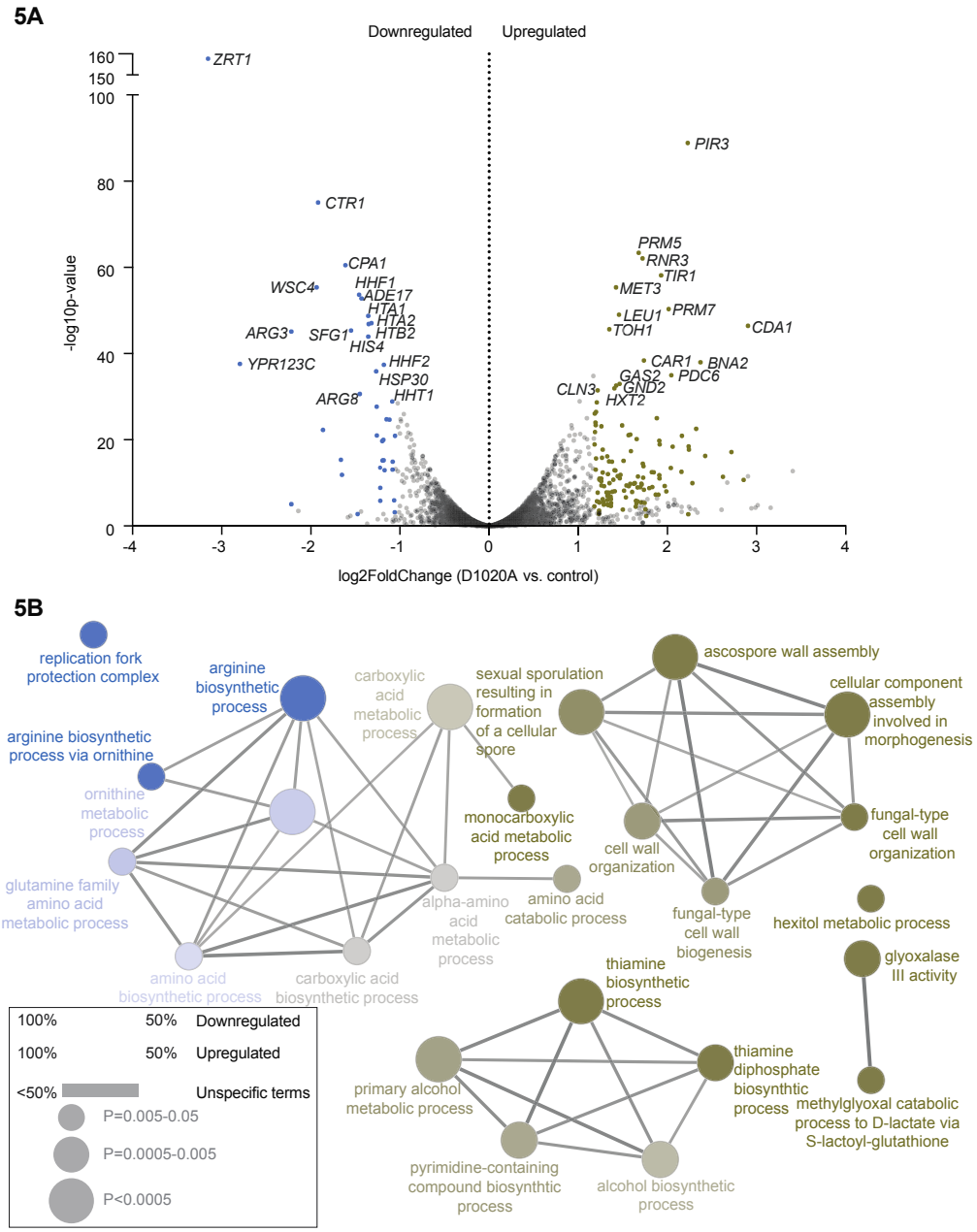

431

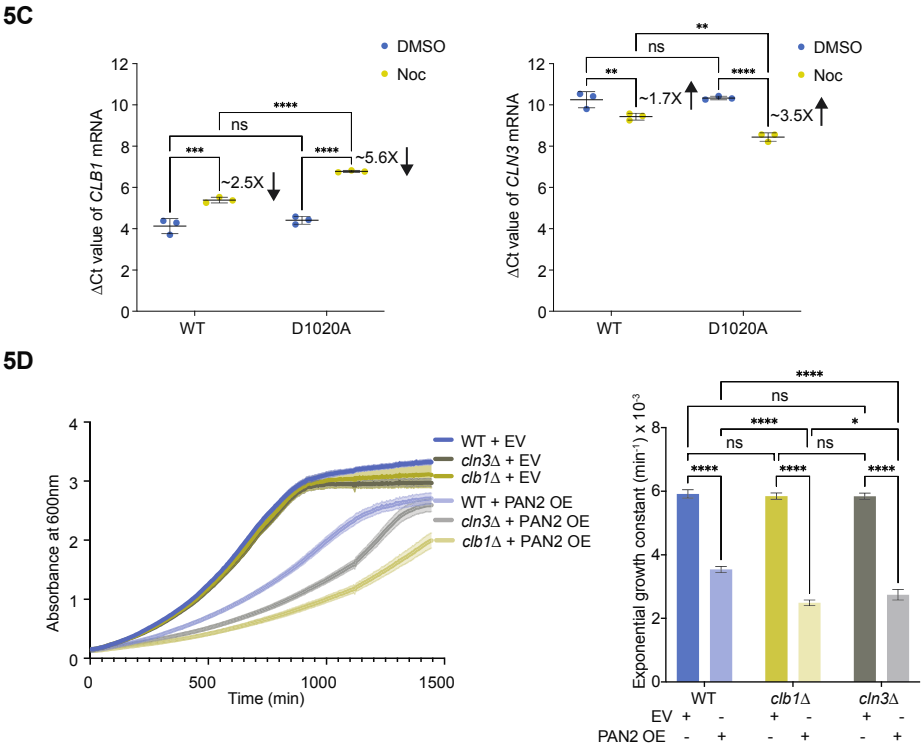

Fig 5: **mRNA levels of *CLB1* and *CLN3* are altered in deadenylase dead mutant of *PAN2* in nocodazole. (A)** Fold change and p-value of ~6000 ORFs analyzed in nocodazole treated Control and D1020A cells by RNA-sequencing. Each closed circle represents a single ORF, categorized into upregulated (green), downregulated (blue) or not-significantly different (gray) (**B**) Functional enrichment of the upregulated and downregulated genes identified in (**A**). Node size indicates statistical significance of enriched GO terms and edges indicate statistically significant associations between terms. Node color indicates the % of aggravating or alleviating interactions in each term. Unspecific terms in gray. (**C**) Gene expression changes in *pan2*Δ+WT-PAN2 or *pan2*Δ+D1020A-PAN2 post 6 hour treatment with DMSO or 6 μM nocodazole

442 assessed by qRT-PCRs. The ΔCt values are normalized to actin. Data mean +/- S.D. 0.4X and
443 2X indicate fold-change in *CLB1* and *CLN3* mRNA levels respectively. n.s., not significant;
444 **** $p < 0.0001$; *** $p < 0.001$; **, $p < 0.01$. Two-way ANOVA for significant differences. Ct,
445 cycle threshold; μM, micromolar; qRT, quantitative reverse transcriptase; ANOVA, Analysis of
446 Variance. (**D**) Growth curves of yeast strains grown in liquid SC media and monitored for 24
447 hours at 30°C. Absorbance adjusted for baseline correction is plotted on the y-axis and time (in
448 minutes) is plotted on the x-axis. An average of 6 replicates have been plotted with SD. min,
449 minutes; SC, Synthetic Complete media; SD, standard deviation; WT, wild type; EV, empty
450 vector; OE, overexpression. Base 2 exponential growth constants calculated from growth of
451 different yeast strains. Error bars are +/- SD from three separate experiments. Each experiment
452 has 6 replicates. Significant differences between different strains were tested using two-way
453 ANOVA comparison.
454
455 Two genes, *CLN3* and *CLB1*, with functions related to regulation of cyclin-dependent protein
456 serine/threonine kinase (CDK) activity, were significantly different between WT and D1020A
457 Pan2 treated with nocodazole. *CLN3* encodes a CDK regulatory subunit that regulates cell-cycle
458 passage through START by regulating transcription at the G1/S transition. *CLB1* encodes a B-
459 type cyclin involved in the regulation of the G2/M transition of both the mitotic cell-cycle and
460 first meiotic division (40). *CLB1* is also involved in mitotic spindle assembly and spindle pole
461 body separation through its interaction with CDK1 (41). By qPCR we found that *CLB1* mRNA
462 levels decreased ~2.5 fold in cells with WT Pan2 in response to nocodazole, whereas in cells
463 with D1020A Pan2, *CLB1* decreased ~5.6 fold (**Fig 5C**). There was no difference in *CLB1*
464 expression between cells with WT or D1020A Pan2 in the absence of nocodazole. Similarly, for

CLN3 there was no difference between cells with WT or D1020A Pan2 in the absence of nocodazole, however in the presence of nocodazole *CLN3* mRNA levels increased ~1.7 fold in cells with WT Pan2 and ~3.5 fold in cells with D1020A Pan2 (**Fig 5C**). Thus, PAN was required for regulation of *CLB1* and *CLN3* mRNA levels in response to nocodazole.

Given the changes we observed in *CLB1* and *CLN3* expression in cells with D1020A Pan2, we tested for functional associations between PAN and *CLB1* and *CLN3*. We constructed double mutants between *PAN2* and *CLB1* and *CLN3* and tested for genetic interactions in the absence and presence of nocodazole. Growth of the double mutants was the same as the *PAN2* single mutant both in the absence and presence of nocodazole, indicating deletion of either *CLB1* or *CLN3* did not modify the Δ*pan2* nocodazole sensitivity (**Fig S5B**). Next we tested overexpression of *PAN2* in the absence of *CLB1* or *CLN3*. Similar to HsPAN2, overexpression of yeast *PAN2* caused a slow growth phenotype in WT yeast (**Fig 5D**). This phenotype was enhanced in cells lacking *CLB1* and *CLN3* (**Fig 5D**), indicating a functional association between PAN and both *CLB1* and *CLN3*. Thus, these data supported that the role for PAN in response to microtubule stress involved regulation of Clb1 and Cln3 function.

PAN2 depletion in mammalian cells increases sensitivity to microtubule destabilizing drugs

To determine if the function of Pan2 in regulating the cell-cycle upon microtubule stress is conserved from yeast to mammalian cells, we implemented a human cell culture system to examine sensitivity to microtubule destabilizing drugs and spindle integrity. We generated a population of HEK293 cells where Pan2 was stably knocked down using an shRNA targeting the ORF of *PAN2* (**see Methods**). Specifically, we observed ~ 75% reduction in protein levels of Pan2 by western blot in this population (**Fig 6A**).

491 Figure 6

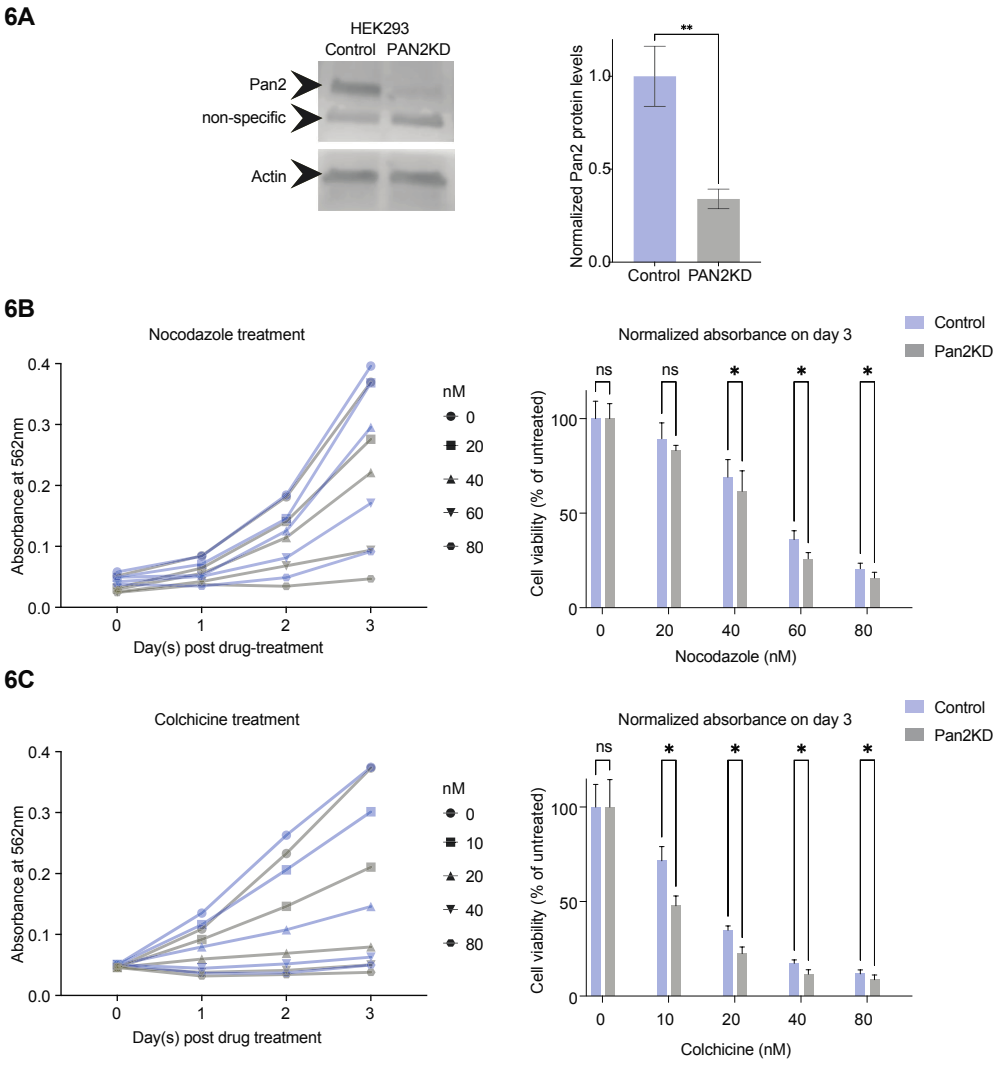

492

493 **Fig 6: HEK293 PAN2KD cells are sensitive to nocodazole and colchicine.** (**A**) Cell lysates

494 from HEK293 Control and Pan2KD cells were analyzed on an SDS gel and probed for Pan2 and

495 Actin levels, quantification for which is shown on right, n=3. Significant differences between the

496 2 strains were tested using paired Student's *t*-test. **, $p < 0.01$. (**B-C**) Absorbance at 562 nm (y-

497 axis) and days post treatment (x-axis) with nocodazole **(B)** or colchicine **(C)** was plotted for
498 control (blue) and Pan2KD (gray) at various concentrations of drug. Absorbance of each treated
499 condition was normalized to the absorbance of the untreated condition for each cell line on the
500 day 3 post-treatment to plot cell viability (% of untreated). Average of 6 replicates has been
501 plotted. Mean +/- S.D. Significant differences between Control and Pan2KD cells at each
502 concentration was tested using multiple Student's *t*-test. nM, nanomolar; n.s., not significant; *,
503 $p<0.05$.
504
505 To determine if this reduction in Pan2 reduced viability and/or slowed the growth of cells treated
506 with the microtubule inhibitors nocodazole or colchicine, we used a colorimetric MTT (3-(4, 5-
507 dimethylthiazol-2)-2, 5-diphenyltetrazolium bromide) assay for live, metabolically active cells
508 that reads out as absorbance at 562 nm (42). We seeded wells at 1,000 cells per well, added drug
509 16 h later and at a further 0, 24, 48 and 72 h we performed MTT assay (**Fig S6A**). We observed a
510 dose-dependent decrease in cell viability as measured by A562 in both control and Pan2KD cells
511 treated with nocodazole or colchicine over the time course (**Fig 6B &C, left panels**). We
512 compared the viability of Pan2KD and control cells at the endpoint of the assay on day 3. For
513 nocodazole treatment, we observed a significant decrease in viability of Pan2KD compared to
514 control cells at 40, 60 and 80 nM nocodazole (**Fig 6B, right panel**). For colchicine we observed
515 significant decreases at all concentrations (**Fig 6C, right panel**). This suggested that, as was the
516 case in yeast, depletion of Pan2 increased the vulnerability of mammalian cells to microtubule
517 depolymerization.
518

519 Figure S6

S6A

520
521
522
523
524 **Fig S6A**: Protocol for recording MTT activity of cells over multiple days.
525

526 **PAN2KD cells exhibit extended metaphase and multipolar spindle formation upon**
527 **treatment with colchicine**

528

529 We were curious to determine the cause of increased sensitivity of HEK293 Pan2KD cells to
530 microtubular depolarization and how this related to the cell-cycle. Thus, we live-imaged
531 microtubules in the control and Pan2KD cells using a tubulin staining dye, CellLight™ Tubulin-
532 RFP BacMam 2.0. Upon treatment with a low dose of 10 nM of colchicine, we imaged cells for a
533 period of 24 hours to capture the spindle morphology, as well as to determine the duration of
534 different stages of mitosis (**Fig S7A**). In the absence of drug treatment, progression through the
535 cell-cycle appeared normal for both control and Pan2KD cells (**Fig 7A; also see movie SFile 8**).
536 We observed no differences in metaphase duration or spindle morphology. In contrast, upon
537 treatment with 10 nM colchicine, as compared to control cells, Pan2KD showed abnormal
538 progression through the cell-cycle (**Fig 7A; also see movie SFile 9**). Pan2KD cells spent longer
539 time in metaphase (**Fig 7A**) and had a higher propensity to form multipolar spindles (~75% in

Pan2KD vs ~40% in Ctrl) (**Fig 7A**; also see 100 min image in **Fig 7A**). This indicated that Pan2 played a role in spindle integrity during microtubule stress and was consistent with the decreased viability we observed in Pan2KD cells treated with nocodazole and colchicine.

543 Figure S7

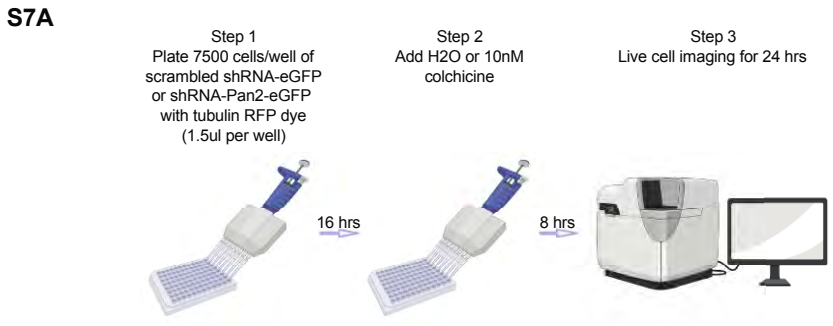

544
545

546 **Fig S7A**: Protocol for live-cell imaging of colchicine treated cells using tubulin staining dye.

547

548 Figure 7

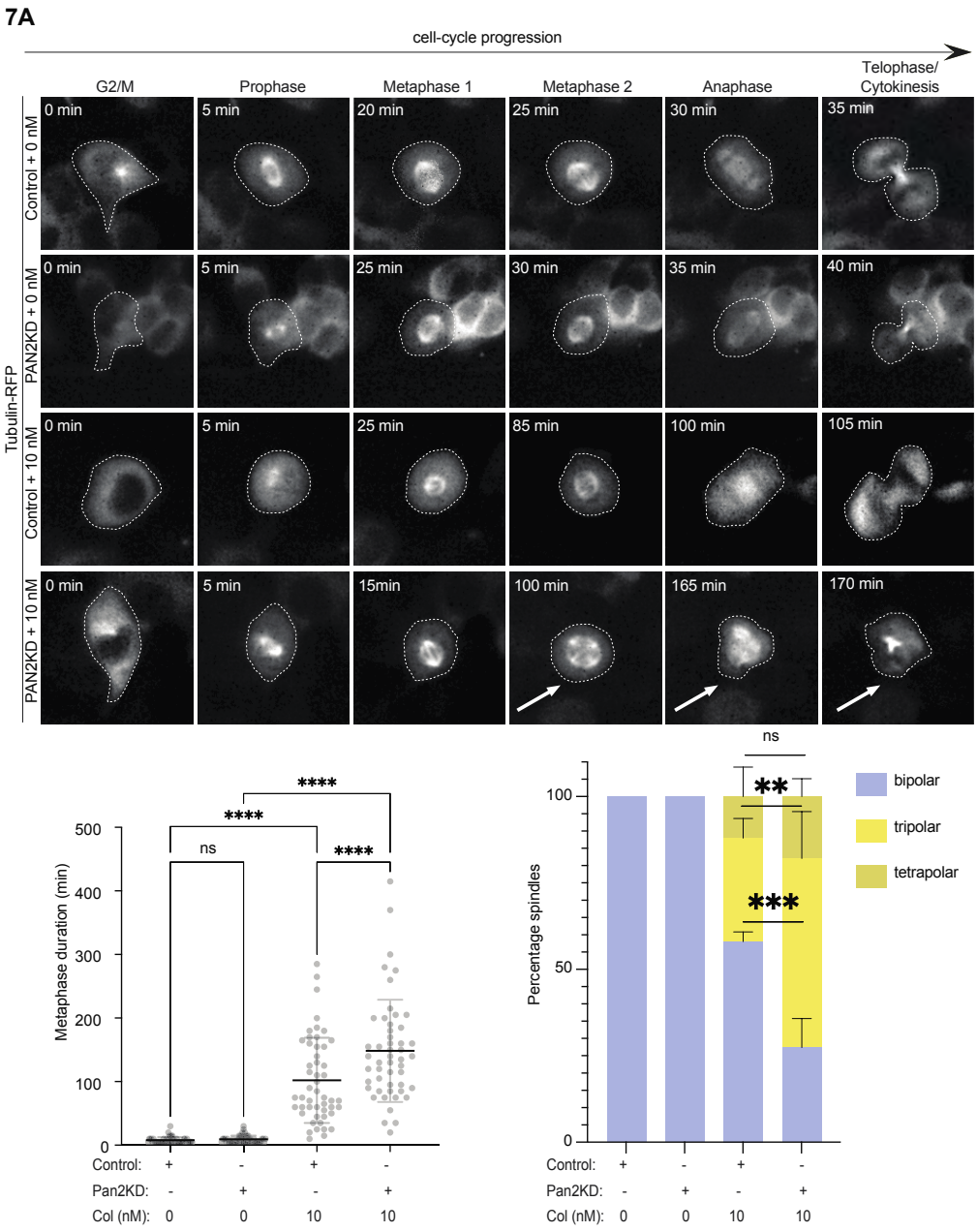

549

Fig 7: **HEK293 PAN2KD cells exhibit defective spindle phenotypes upon treatment with colchicine** (**A**) Representative images of HEK293 Control and Pan2KD cells with or without treatment with 10 nM colchicine. These cells are shown undergoing mitosis at the transition from G2 to M and different phases of M-phase (prophase, metaphase 1, metaphase 2, anaphase and telophase). The time taken for each stage of mitosis is indicated on top left of each snapshot. Arrows indicate cells with multipolar spindles. Metaphase duration (in minutes) and percentage of cells having 2, 3 or 4 spindles is plotted for colchicine treatment of HEK293 Control and Pan2KD cells. Each closed circle represents one cell. 50 cells were counted for each condition. Mean +/- S.D. has been plotted. nM, nanomolar; min, minutes; ns, not significant; **, $p<0.01$; ***, $p<0.001$; ****, $p<0.0001$.

Discussion

Since the role of PAN in response to microtubule stress was dependent on its deadenylase activity, we propose that PAN regulates the PATLs of mRNAs required for cellular survival of microtubule stress (**Fig 8**). PAN activity during microtubule stress would lead to translational repression of key proteins involved in either sensing microtubule stress and/or responding to/recovering from formation of defective spindles. Some obvious targets are proteins involved in the spindle assembly checkpoint, however we did not find expression of any of these to be altered in our mRNA seq screen. We also did not detect altered expression of genes with functions directly related to microtubule biogenesis, including the tubulin genes themselves, making it unlikely that PAN regulates microtubules directly. However, it is possible that our screen missed these targets because it did not identify mRNAs with altered poly-A tail lengths.

573 Altered poly-A tail length could lead to altered translation, independent of mRNA stability,
574 hence screening for altered poly-A tail length would likely produce novel insights into PAN's
575 mechanism of action (15,43). It is interesting that cells lacking PAN appear to have a normal
576 cell-cycle, normal spindles, and show no decrease in fitness under regular growth conditions.
577 This further supports a specific role for PAN in response to microtubule/spindle stress and
578 perhaps explains its elusive role in the cell-cycle until now.

579 Figure 8

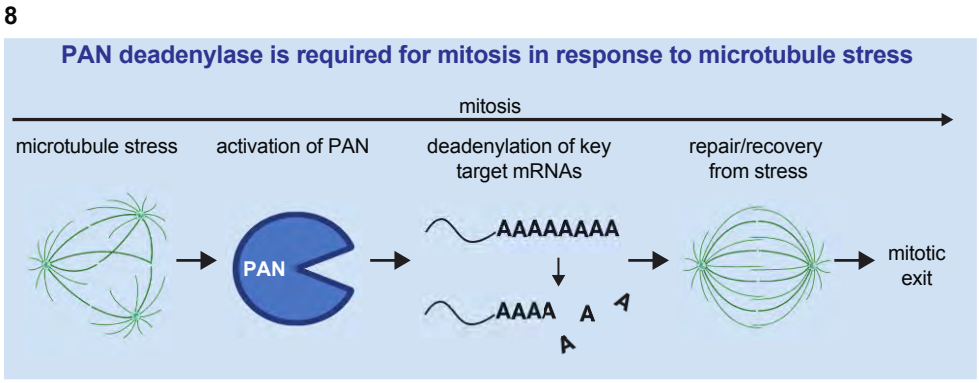

580

581 **Fig 8**: Model schematic of PAN regulating the mRNA polyA tails lengths (PATLs) of mRNAs

582 required for cellular survival of microtubule stress.

583

584 We did identify a functional connection between PAN and two important cell-cycle regulators,

585 Clb1 and Cln3, although the significance remains obscure. Decreased expression of *CLB1* in

586 response to nocodazole is consistent with failure of Δ*pan2* cells to complete mitosis, however

587 because *CLB1* is decreased in Δ*pan2* cells it is unlikely to be a direct target. The fact that *CLB1*

588 expression increases in response to nocodazole in WT yeast (which complete mitosis apparently

589 normally) supports that *CLB1* is part of the microtubule stress response. This is also supported by

590 the genetic interaction we observed between PAN and *CLB1*. It is possible that the low

591 expression of *CLB1* in Δ*pan2* cells treated with nocodazole prevents completion of mitosis,

592 however we might have expected to see loss of *CLB1* enhance the nocodazole sensitivity of

593 Δ*pan2* cells, which wasn't the case. It is possible that *CLB1* expression is already limiting, in

which case overexpression of *CLB1* should reduce the nocodazole sensitivity of Δ*pan2* cells if Clb1 is playing an important role in the response. *CLN3* expression was found to be upregulated in response to nocodazole which was enhanced in Δ*pan2* cells. Since Cln3 is not known to play roles in mitosis it is unclear why Cln3 is being impacted. If *CLN3* was a direct target of PAN and its elevated expression was preventing completion of mitosis, we would have expected loss of *CLN3* to suppress the nocodazole sensitivity of Δ*pan2* cells, which wasn't the case. Because we identify a genetic interaction between PAN and *CLN3* it is likely Cln3 is functionally relevant, perhaps indirectly by affecting cell-cycle dynamics or by regulating PAN activity outside of M phase.

There is evidence for regulation of cell-cycle progression through regulation of PATLs. For example, genes such as *CDK1, TOP2A, KPNA2, UBE2C* and *FBXO5*, which orchestrate timing and coordination of mitotic events in somatic cells, have been found to have reduced PATLs in M-phase (15). Transcription of these genes peaks at G2/M phase and is repressed at G1 phase (44). In contrast, other well-known mitotic regulators which are also transcriptionally upregulated in G2/M phase, such as *CCNA, CCNB*, and *CENP-E*, do not show poly(A) length changes (44). This suggests that a subset of genes are selectively deadenylated to shut down once cells enter M phase. Specifically, *CDK1* displayed the most extreme change, whose median poly(A) tail length changed from 77 nt in S phase to 2 nt in M phase and displayed translational repression (15), unlike the previous report showing translational upregulation of *CDK1* in M phase (45). Analysis of gene ontology for genes exhibiting shortened poly(A) tails during the M phase identified enriched terms such as "regulation of mitotic cell-cycle", "microtubule cytoskeleton", and "regulation of ubiquitin-protein ligase activity". This implies that

deadenylation during the M phase may be linked to regulatory functions within the cell cycle. It is currently unknown which deadenylases are responsible for which modifications and our results suggest that PAN may play an important role. Ccr4-Not may also play a role, however, the fact that loss of Ccr4-Not activity in yeast does not lead to sensitivity to microtubule destabilizing drugs implies a prominent function for PAN (29).

Post-transcriptional regulation of mRNAs plays a critical role during the cell cycle and can be achieved through their localization to specific subcellular compartments (46–48). A high-throughput smFISH (single molecule Fluorescence *In Situ* Hybridization) screen of 602 proteins with centrosomal functions identified 8 human mRNAs (*NIN, CEP350, PCNT, BICD2, CCDC88C, ASPM, NUMA1,* and *HMMR)* that are locally translated at the centrosome (49). Seven of these are translated during mitosis (*CCDC88C* is translated only during interphase). *CEP350, ASPM, NUMA1,* and *HMMR* are microtubule binding proteins with functions in centrosome/spindle maturation and *NIN, PCNT* and *BICD* contribute to microtubule anchoring at the centrosome (50–56). Hence, these proteins are potential PAN targets in response to microtubule stress. However, we did not find altered levels of yeast spindle pole body mRNAs in our RNA-seq screen, suggesting either we missed detecting such changes or that PAN acts via other targets. Given that the yeast spindle pole body shares no structural similarity to the centrosome and that RNAs have yet to be localized to spindle pole bodies further suggests that PAN targets components other than the centrosome/spindle pole body in yeast and humans.

The spindle phenotypes we observed in Pan2KD cells treated with colchicine coupled with their decreased cell viability suggested these cells could have undergone abnormal chromosome

segregation. Cells with mis-segregated chromosomes often have abnormal nuclei and have increased cell death (57–59). An imaging based whole-genome siRNA screen in HeLa cells found that the absence of *PAN2* led to irregular nuclear shape and chromosome mis-segregation (60). Upon chromatin extraction during G2, Pan2 and Pan3 were found to be part of a soluble complex containing the spindle checkpoint proteins Bub1 and Mad1l1, the kinetochore proteins Ndc80 and Nuf2, and 265 other proteins enriched for the molecular functions poly(A)-specific ribonuclease activity, poly(A) binding, translation initiation factor activity, mRNA 3'UTR binding, RNA-helicase activity, ribosome binding, microtubule motor activity and gamma-tubulin binding (60). Hence, this study provides evidence that PAN's role in responding to microtubule stress may involve direct associations between PAN complex and key spindle regulatory proteins, which is required for proper chromosome segregation.

Previous studies have shown that the PAN localizes to P-bodies in yeast cells. P-bodies serve as sites of mRNA storage, decay, and translational repression. Sweet et al. find that treating yeast with the microtubule depolymerizing drug benomyl induces formation of P-bodies containing tubulin (61). However, according to the HIPHOP chemical genetics database (29), none of the P-body protein mutants are sensitive to nocodazole or benomyl, suggesting the role for PAN in microtubule stress is independent of P bodies. Additionally, many groups have reported an increase in P-body numbers during S phase, the disappearance of PB structures before mitosis, and their reassembly during cytokinesis in mammalian cells, further supporting a non-P body role for PAN during mitosis (62,63).

Finally, if the role of PAN is restricted to responding to microtubule stress in M-phase, this raises the question of whether PAN activity is regulated in a cell-cycle dependent manner and/or in response to stress. Pan3 has previously been identified as a substrate of the CDK Pho85 (24). Different groups have identified 9 phosphorylation sites on Pan3, one in the pseudokinase domain and the rest in unstructured regions. Holt et al. identified residue 415 in the linker domain of Pan2 as a substrate of CDK1 phosphorylation (22). Phosphorylation of Pan3 in mammalian cells has previously been shown to decrease its interaction with PABPC1 and reduce PAN activity (23). Together this suggests PAN activity is regulated by phosphorylation by CDKs in a cell-cycle dependent manner. Interestingly, our SGA screen identified an alleviating genetic interaction between *PAN2* and *PHO85*, supporting a functional connection between PAN and this important cellular stress response regulator. The need for cell-cycle dependent regulation of PAN might also explain our finding that having too much Pan2 in the cell leads to reduced cell growth, although the cause of this fitness defect has yet to be elucidated.

676 **Materials and Methods**

677

678 **Yeast strains, growth conditions, and manipulations**

679

680 Deletion and tagged strains were constructed in JHY716 or BY4741 (derivatives of S288C)
681 backgrounds using homologous recombination of PCR-generated linear fragments amplified
682 from pKT209, pHIS3p:yomWasabi-Tub1+3'UTR::HPH, and pFA6a-kanMX6 (38,64,65), with
683 successful recombination assessed by colony PCR. All yeast strains were maintained on standard
684 yeast growth medium of either yeast extract, peptone, and dextrose (YPD) media or synthetic
685 complete (SC) media consisting of Yeast Nitrogen Base (YNB) supplemented with appropriate
686 amino acids and 2% dextrose. Yeast cultures were grown at 30°C. A complete list of all the
687 strains used in this study is provided in **Table 1**.

688

689 **Table 1: List of strains**

690

Strain	**Genotype**	**Source**	**Parental strain**	**Notes**
BY4741	MAT**a**; *his3Δ1*; *leu2Δ0*; *met15Δ0*; *ura3Δ0*; S288C background	Lab collection		Wild type
BY4742	MAT*α*; *his3Δ1*; *leu2Δ0*; *ura3Δ0*; S288C background	Lab collection		Wild type

Y7092	MAT*α*; *his3Δ1*; *leu2Δ0*; *met15Δ0*; *ura3Δ0*; LYS2+; *can1Δ*::STE2pr-Sp_his5; *lypΔ1*; S288C background	Kind gift from Dr. Charlie Boone		SGA query strain background
JV1	*pan2*Δ::*uraMX*	This study	Y7092	PCR knock-in
JV2	*pan3*Δ::*uraMX*	This study	Y7092	PCR knock-in
JV3	*HIS3pr*:yomWasabi-Tub1+3'UTR::HPH	This study	Y7092	PCR knock-in
JV4	*pan2*Δ::*uraMX* *HIS3pr*:yomWasabi-Tub1+3'UTR::HPH	This study	Y7092	PCR knock-in
JV5	*pan2*Δ::*uraMX cin1*Δ::kanMX6	This study	SGA background	SGA
JV6	*pan2*Δ::*uraMX cin2*Δ::kanMX6	This study	SGA background	SGA
JV7	*pan2*Δ::*uraMX cin4*Δ::kanMX6	This study	SGA background	SGA
JV8	*pan2*Δ::*uraMX gim3*Δ::kanMX6	This study	SGA background	SGA
JV9	*pan2*Δ::*uraMX gim4*Δ::kanMX6	This study	SGA background	SGA
JV10	*pan2*Δ::*uraMX pac2*Δ::kanMX6	This study	SGA background	SGA

JV11	*pan2*Δ::*uraMX tub3*Δ:: kanMX6	This study	SGA background	SGA

691

692 **Plasmids and constructs**

693

694 CEN plasmids were taken from the MoBY-ORF collection (66). Galactose-driven
695 overexpression plasmids were obtained from the FLEX overexpression library (67) generously
696 provided by Tejomayee Singh from the laboratory of Dr. Phil Hieter. All plasmids were
697 sequenced to confirm their identity (Plasmidsaurus). The coding sequence of *Saccharomyces*
698 *cerevisiae PAN2* gene, along with its native promoter and 3'UTR sequence, and the codon
699 optimized version of *Homo sapiens PAN2* (sequence is provided in **SFile 1**) were purchased
700 from Twist Biosciences to insert into various plasmids for tagging or overexpression using the
701 Gateway cloning kit (ThermoFisher Scientific). These plasmids were pAG426*GAL*-ccdB,
702 pAG426-*GAL*-GFP-ccdB, pAG425-*GAL*-ccdB, pAG415-*GPD*-ccdB, and pAG425-*GPD*-ccdB.
703 Details of these plasmids are provided in **Table 2**.

704

705 **Table 2: List of plasmids**

706

Plasmid name	**Description**	**Source**
pKT0209/pKT209	pFA6a–link–yEGFP–Ca*URA3*; used for URA amplification for making gene deletion cassettes	Addgene (64)
pHIS3pr:yomWasabi -Tub1+3'UTR::HPH	*pHIS3pr*:yomWasabi-Tub1+3'UTR::HPH: used for tagging alpha-tubulin	Addgene (38)

pFA6a-kanMX6	for one-step PCR deletion of gene of interest	Addgene (65)
pAG426-*GAL*-Pan2	URA3 marker, multi-copy, GAL promoter	This study
pAG426-*GAL*-Pan2-D1020A	URA3 marker, multi-copy, GAL promoter	This study
pAG426-*GAL*-GFP-Pan2	URA3 marker, multi-copy, GAL promoter, N-terminal GFP-tagging	This study
pAG426-*GAL*-GFP-Pan2-D1020A	URA3 marker, multi-copy, GAL promoter, N-terminal GFP-tagging	This study
pAG425-*GAL*-Pan2	LEU2 marker, multi-copy, GAL promoter	This study
pAG425-*GAL*-Pan2-D1020A	LEU2 marker, multi-copy, GAL promoter	This study
pAG425-*GAL*-HsPan2	LEU2 marker, multi-copy, GAL promoter	This study
pAG415-*GPD*-Pan2	LEU2 marker, low copy, GPD promoter	This study
pAG415-*GPD*-Pan2-D1020A	LEU2 marker, low copy, GPD promoter	This study
pAG425-*GPD*-Pan2	LEU2 marker, multi-copy, GPD promoter	This study
pAG425-*GPD*-Pan2-D1020A	LEU2 marker, multi-copy, GPD promoter	This study
pFLEX-Pan2	*GAL1-10pr, URA3*	A gift from Dr. Phil Hieter (67)

The deadenylase dead mutation (D1020A) in *PAN2*'s coding sequence was generated by site-directed mutagenesis (Q5 Site Directed Mutagenesis Kit from NEB E0554) with primer pairs 5' GGTTTGAATAATGCCTTCAAACACATTAATATTAATGTC 3' and 5' ATGACCAACAAATACATTATTCAAACCATGACCAAC 3'. These PCR products were recombined in DHFpir bacteria which was a generous gift from Dr. J.T. Beatty.

For tagging Tub1 with yomWasabi-Tub1+3'UTR, the strategy used has been described in Markus et al., 2015 (38). Briefly, the yomWasabi-Tub1 tagging plasmid was altered by adding an additional 618 nucleotides corresponding to the region downstream of the *TUB1* locus. This sequence was chosen because it extends well beyond the last potential polyadenylation sequence (AATAAA, 145 nt downstream of the stop codon; ATTAAA, 540 nt downstream of the stop codon). Following transformation with the BsaBI-digested plasmid (*pHIS3p*:yomWasabi-TUB1+3'UTR), both the endogenous, untagged *TUB1* and the tagged *TUB1* genes are immediately followed by the 3'UTR sequence.

Quantitative liquid growth assays

Yeast were grown overnight in liquid SC media supplemented with appropriate amino acids, diluted into fresh medium, then grown until reaching logarithmic growth phase (OD_{600} 0.2-0.5). Yeast cells were then transferred to liquid media supplemented with an appropriate concentration of nocodazole (Sigma) or equivalent percentage (<0.5%) of DMSO (ThermoFisher). Strains were normalized to the same OD_{600} then diluted to an OD_{600} value of 0.005-0.010 in 96-well

plates in triplicate wells to a volume of 200 µL. Plates were then incubated at 30°C with orbital shaking at 600 RPM in a Biotek Instruments Epoch 2 Microplate Spectrophotometer. Data was $\log_2$ transformed and appropriate time points were fitted to a linear equation, with exponential growth constants derived from the slopes of the linear equation (except in drug treatments where yeast showed a non-exponential growth pattern). Statistical analysis was performed in GraphPad Prism 10, and significant differences between pairs were detected using Student's *t*-test or between pairwise combinations of groups using a one-way ANOVA with *post-hoc* multiple comparisons corrections using Tukey's method.

Western blotting

Yeast cell lysates were prepared using the TCA (Trichloroacetic acid) precipitation method (68). The following primary antibodies were used: chicken anti-GFP (1:5000 of Abcam ab13970) and mouse anti-PGK1 (1:5000 of Abcam ab113687). The following secondary antibodies were used: donkey anti-chicken Alexafluor 488 (1:10,000 of Jackson ImmunoReserach Lab 703-545-155) and goat anti-mouse DyLight 800 (1:15,000 of Invitrogen SA5-10176). The experiments were performed in triplicates, and the results were quantified using the Image Lab software (BioRad).

Mammalian cells were lysed using RIPA (Radio Immuno Precipitation Assay) buffer (50 mM Tris–HCl (pH 7.4), 150 mM NaCl, 1% Triton X-100, 0.5% sodium deoxycholate, 0.1% SDS, and 5 mM EDTA) supplemented with cOmplete protease inhibitors (Roche). The following primary antibodies were used: rabbit anti-PAN2 (1:1000 of Proteintech 16427-1-AP) and mouse

752 anti-actin (1:5000 of Abcam ab8226). The following secondary antibodies were used: goat anti-

753 mouse HRP (Jackson 115-035-003) and goat anti-rabbit HRP (Jackson 111-035-003).

754

Synthetic Genetic Array Analysis

Creation of the genome-wide array of double mutants with the *pan2*Δ deletion strain was undertaken as previously described (69,70). Briefly, *PAN2* was knocked-out in the SGA query strain background Y7092 by genomic integration of the *URA3* cassette at the *PAN2* genomic locus amplified from pKT209. This *pan2*Δ query strain was mated to an array of non-essential deletion mutants marked with kanMX6 using a Singer RoToR HDA robot. Diploids were selected for and induced to undergo sporulation. From spores, *MAT***a** cells were obtained by pinning onto haploid selection media (SC-His/Arg/Lys supplemented with 100 µg/mL canavanine and 100 µg/mL thialysine). Control plates were obtained by re-pinning to 5-FOA media to counter select for the *PAN2* deletion, while experimental plates were generated by plating on media lacking uracil. These were then separately pinned onto plates containing 1.5µM of nocodazole. Plates were imaged using a CanoScan flatbed scanner and were analyzed using Balony software (69). Gene Ontology (GO) term enrichment and protein-protein interaction network analysis was performed using the GeneMANIA web server, with GO term enrichment presented as Benjamini-Hochberg FDR-adjusted p values (q values) from hypergeometric tests (71,72).

FACS analysis of DNA content

Yeast cells were cultured under specified conditions, fixed in 70% ethanol, and stored at 4°C. Fixed cells were rehydrated in phosphate-buffered saline, incubated with 100 µg/mL RNase A (ThermoFisher) for 3 hrs, and stained with 5 µg/mL propidium iodide (Invitrogen) for 1 hour.

Cells were analyzed using a Cytoflex LX Analyser, and yeast cells were separated from debris by gating with forward scatter and side scatter. The experiments were repeated three times using freshly grown cultures.

Confocal microscopy

Log phase (OD_{600} 0.2-0.5) yeast cells were centrifuged at 2,000 g and imaged in sterile filtered SC liquid medium (yeast nitrogen base without amino acids and with ammonium sulphate, amino acid mix, dextrose). Squashes of yeast were made and imaged on the Leica SP5 system with DIC imaging. Images were analyzed using the Fiji distribution (73) of ImageJ software (74).

Sample preparation for live-cell imaging of yeast and cell-segmentation

Live-cell imaging of yeast was conducted in Concanavalin A (ConA) (Sigma L7647) coated 96-well microscope dishes using the Cell Discoverer 7 imaging system. To prepare the ConA-coated dishes, a stock solution of ConA at a concentration of 10 mg/mL was initially prepared and stored in aliquots at -20°C for a maximum of 6 months. A working solution was then prepared by diluting the stock to a final concentration of 1 mg/mL and stored at 4°C for several weeks. The ConA solution was evenly applied to each well of the 96-well dishes (Cellvis, P96-1.5H-N). Following a 5-minute incubation on the benchtop, excess solution was aspirated, and the dishes were allowed to dry for 5 minutes. For sample preparation, yeast cultures were grown overnight in SC medium (sterile filtered). The following day, yeast cultures were diluted and allowed to

grow to log phase. Cells were adhered to the ConA-coated plates by applying 20 µL of the cell suspension to each well. After 10 minutes of incubation to ensure proper adhesion, the media was removed, and 40 µL of fresh media without cells was added to eliminate potential optical artifacts. The CellDiscoverer7 (Carl Zeiss) microscope was set up prior to starting the live-cell imaging to reach 30°C and allow the objectives to acclimate to that temperature. An imaging time course was set up using ZEN Blue software (Carl Zeiss) to take images at 2 evenly dispersed, non-overlapping locations per well. For each condition, 2 biological replicates were imaged in separate wells. Images were taken in brightfield (TL LED lamp) and GFP (LED module 470nm) channels. The Plan Apochromat water immersion 50x/1.2 objective and 1x Tubelens were used for a final magnification of 50x, with an effective NA of 1.2. Images were taken every 5 minutes for 480 minutes using definite focus. The individual images were deconvolved using the constrained iterative algorithm and max intensity images were generated using extended depth of focus with an effective depth of ~1µm (9 z-stacks of ~0.125µm). Images were analyzed using the ZEN Blue software (Carl Zeiss). GFP segmentation was performed to collect data for individual cells after Gaussian smoothing, sigma=2, using iso data thresholding for light regions. For each GFP segmented cell, area and GFP mean intensity were measured. Data for the cells in each of the 4 images per well were compiled to generate the total cell number, number of dead cells (brighter, GFP mean intensity > 8000) and cell area.

RNA isolation and qRT-PCR analysis

Total RNA was isolated from cells using the RNeasy kit from Qiagen (74104) following the manufacturer's instructions. Quantitative reverse-transcriptase PCR was performed using Power

SYBR® Green RNA-to-CT™ 1-Step Kit from ThermoFisher (4389986). All data were normalized to *ACT1* transcript levels and are presented as ΔCt values. Where a statistically significant change was observed, fold-increase against control was indicated in the plots. The primers used in this study are listed in **Table 3**.

Table 3: RT-PCR primers

Primer	**Sequence**
Sc_Act1_qFwd	TTTGCCGGTGACGACGCTCC
Sc_Act1_qRev	ACAGGGTGTTCTTCTGGGGCA
Sc_Clb1_qFwd	CAGTCTAGGACGTTAGC
Sc_Clb1_qRev	GTCGTGAATAGTAGATCC
Sc_Cln3_qFwd	TCAGCGCTGCCTCATGTC
Sc_ Cln3_qRev	ATGGCCCGCCTCTTTTG
Sc_ Tub1_qFwd	GGCCACTGTGGATAGGGCCG
Sc_ Tub1_qRev	TCAGCGTATGAGTCGGCACCC
Sc_ Tub2_qFwd	CGTCGATCTAGAACCTGGGA
Sc_ Tub2_qRev	GACGCTGTCTACAAGCTCAG
Sc_ Tub3_qFwd	TGGCCGACCAATGTGACGGT
Sc_ Tub3_qRev	AGGCGCAGGATAAACGGCGA

RNA sequencing and analysis

Sample quality control was performed using the Agilent 2100 Bioanalyzer. Qualifying samples were then prepped following the standard protocol for the Illumina Stranded mRNA prep (Illumina). Sequencing was performed on the Illumina NextSeq2000 with Paired End 59bp × 59bp reads by BRC-sequencing facility. As previously described (75), multiple differential expression analysis pipelines were applied, and the results combined. The pipelines used the reference genome and transcriptome R64-1-1 downloaded from Ensembl (www.ensembl.org, Release 107).

Generation of stable PAN2 knockdown mammalian HEK293 cell populations

HEK293A cells were cultured in DMEM/F12 medium (Sigma) supplemented with 10% FBS and grown in an incubator at 5% CO_2 and 37°C and transfected with Dharmacon pGIPZ shRNA set (RHS4531-EG9924; shRNAs fused to GFP) targeting PAN2 ORF/3'UTR using Lipofectamine 2000 according to the manufacturer's protocol (ThermoFisher Scientific 11668027). Puromycin selection was initiated 48 hours post-transfection at a concentration of 1 µg/mL to generate stably integrated shRNA-mediated knockdowns. After 14 days of selection, the puromycin-resistant cells were subjected to FACS to isolate a stably transfected population of GFP-positive cells. Pan2 knockdown efficiency was then determined by Western blotting (1:1000 of Proteintech 16427-1-AP against human Pan2).

Mammalian cell viability assessment using MTT

HEK293 cells were plated in 96-well plates at 10,000 cells/well. The number of viable cells was quantified using a 3-(4,5-dimethylthiazol-2-yl)-2,5-diphenyltetrazolium bromide (MTT; M2128, Sigma) assay at 0, 24, 48, and 72 h. After the designated treatment period, the culture medium was removed, MTT was added to each well at 1 mg/mL in regular growth media for 2 h to allow the formation of formazan crystals (purple precipitate). Following incubation, the MTT solution was aspirated, and the formazan crystals were solubilized using 100 µL of DMSO per well. The plate was gently agitated to ensure complete dissolution of the formazan crystals. The absorbance was measured at 560 nm using a spectrophotometer plate, with DMSO serving as the blank control. Cell viability was calculated as the percentage of viable cells relative to the untreated control group, and the results were expressed as mean ± standard deviation (SD) of at least three independent experiments. Statistical analysis was performed in GraphPad.

Live-cell imaging of mammalian cell spindle formation and mitosis

For spindle analysis of living cells, cells were grown in a 96-well plate (Corning) and a tubulin staining dye, CellLight™ Tubulin-RFP BacMam 2.0 was added prior to imaging the cells in a 37°C and 5% CO_2 environmental chamber (ImageXpress Micro XL). Images were taken using a 40X 0.75 NA dry objective with the MetaXpress 5.0.2.0 software on the ImageXpress Micro XL epifluorescence microscope (Molecular Devices Inc.). Images were taken every 15 minutes using 100-ms exposures, 2x2 binned resolution, with 25% of full lamp intensity per channel. Movies of the fluorescence channels were made in the MetaXpress 5.0.2.0 software (Molecular Devices Inc.).

Acknowledgements

We thank members of the Loewen and Roskelley labs for critical discussions. We thank Dr. Phil Hieter and Dr. J. Thomas Beatty for sharing reagents. We thank the following core facilities at UBC: LSI imaging facility, ubcFLOW, and School of Biomedical Engineering (SBME) Sequencing Core (formerly BRC-Seq). Research was funded by the Canadian Institutes of Health Research (PJT-152967) and CFI Innovation Fund (2020) #39914 awarded to CJRL. This study was partially funded by the Canadian Institutes of Health Research (CIHR 169111) awarded to CDM and Canadian Institutes of Health Research (PJT-162253) awarded to LJH.

Author contributions

JV, CDR and CJRL designed the experiments. JV performed the majority of the experiments. ZH collected live-cell imaging data for HEK293 cells, under the supervision of CDM. JARB collected the flow-cytometry data for cell-cycle analysis in yeast cells, under the supervision of LJH. PD confirmed HEK293 Pan2KD GFP positive cells by flow cytometry. BPY performed the initial testing of sensitivity of *pan2*Δ to nocodazole. SF performed the bioinformatics analysis on RNA-seq data. JV, ZH, JARB, PD, BPY, CDM, CDR and CJRL analyzed the data. JV and CJRL wrote the manuscript. CDM and CDR edited the manuscript.

Competing interests

The authors declare no competing financial interests.

902 **References**

903

904 1. Jackson RJ, Standart N. Do the poly(A) tail and 3′ untranslated region control mRNA
905 translation? Cell. 1990;62(1):15–24.
906 2. Sachs AB, Kornberg RD. Purification and characterization of polyadenylate-binding protein.
907 Methods Enzym. 1990;181:332–52.
908 3. Zlotorynski E. The short tail that wags the mRNA. Nat Rev Mol Cell Biol. 2018;19(1):2–3.
909 4. Nicholson AL, Pasquinelli AE. Tales of Detailed Poly(A) Tails. Trends Cell Biol.
910 2019;29(3):191–200.
911 5. Tang TTL, Passmore LA. Recognition of Poly(A) RNA through Its Intrinsic Helical Structure.
912 Cold Spring Harb Symp Quant Biol. 2020;84:039818.
913 6. Passmore LA, Coller J. Roles of mRNA poly(A) tails in regulation of eukaryotic gene
914 expression. Nat Rev Mol Cell Biol. 2022;23(2):93–106.
915 7. Edmonds M, Vaughan MH, Nakazato H. Polyadenylic Acid Sequences in the Heterogeneous
916 Nuclear RNA and Rapidly-Labeled Polyribosomal RNA of HeLa Cells: Possible Evidence for a
917 Precursor Relationship. Proc Natl Acad Sci. 1971;68(6):1336–40.
918 8. McLaughlin CS, Warner JR, Edmonds M, Nakazato H, Vaughan MH. Polyadenylic Acid
919 Sequences in Yeast Messenger Ribonucleic Acid. J Biol Chem. 1973;248(4):1466–71.
920 9. Weill L, Belloc E, Bava FA, Méndez R. Translational control by changes in poly(A) tail
921 length: recycling mRNAs. Nat Struct Mol Biol. 2012;19(6):577–85.
922 10. Jalkanen AL, Coleman SJ, Wilusz J. Determinants and implications of mRNA poly(A) tail
923 size – Does this protein make my tail look big? Semin Cell Dev Biol. 2014;34:24–32.
924 11. Boeck R, Tarun S, Rieger M, Deardorff JA, Müller-Auer S, Sachs AB. The Yeast Pan2

925 Protein Is Required for Poly(A)-binding Protein-stimulated Poly(A)-nuclease Activity ∗. J Biol
926 Chem. 1996;271(1):432–8.
927 12. Brown CE, Tarun SZ, Boeck R, Sachs AB. PAN3 Encodes a Subunit of the Pab1p-
928 Dependent Poly(A) Nuclease in Saccharomyces cerevisiae. Mol Cell Biol. 1996;16(10):5744–53.
929 13. Yamashita A, Chang TC, Yamashita Y, Zhu W, Zhong Z, Chen CYA, et al. Concerted action
930 of poly(A) nucleases and decapping enzyme in mammalian mRNA turnover. Nat Struct Mol
931 Biol. 2005;12(12):1054–63.
932 14. Yi H, Park J, Ha M, Lim J, Chang H, Kim VN. PABP Cooperates with the CCR4-NOT
933 Complex to Promote mRNA Deadenylation and Block Precocious Decay. Mol Cell.
934 2018;70(6):1081-1088.e5.
935 15. Park JE, Yi H, Kim Y, Chang H, Kim VN. Regulation of Poly(A) Tail and Translation
936 during the Somatic Cell Cycle. Mol Cell. 2016;62(3):462–71.
937 16. Jonas S, Christie M, Peter D, Bhandari D, Loh B, Huntzinger E, et al. An asymmetric PAN3
938 dimer recruits a single PAN2 exonuclease to mediate mRNA deadenylation and decay. Nat
939 Struct Mol Biol. 2014;21(7):599–608.
940 17. Schäfer IB, Rode M, Bonneau F, Schüssler S, Conti E. The structure of the Pan2–Pan3 core
941 complex reveals cross-talk between deadenylase and pseudokinase. Nat Struct Mol Biol.
942 2014;21(7):591–8.
943 18. Wolf J, Valkov E, Allen MD, Meineke B, Gordiyenko Y, McLaughlin SH, et al. Structural
944 basis for Pan3 binding to Pan2 and its function in mRNA recruitment and deadenylation. EMBO
945 J. 2014;33(14):1514–26.
946 19. Yang S, Liu L, Cao C, Song N, Wang Y, Ma S, et al. USP52 acts as a deubiquitinase and
947 promotes histone chaperone ASF1A stabilization. Nat Commun. 2018;9(1):1285.

948 20. Gao M, Guo G, Huang J, Kloeber JA, Zhao F, Deng M, et al. USP52 regulates DNA end
949 resection and chemosensitivity through removing inhibitory ubiquitination from CtIP. Nat
950 Commun. 2020;11(1):5362.
951 21. Christie M, Boland A, Huntzinger E, Weichenrieder O, Izaurralde E. Structure of the PAN3
952 Pseudokinase Reveals the Basis for Interactions with the PAN2 Deadenylase and the GW182
953 Proteins. Mol Cell. 2013;51(3):360–73.
954 22. Holt LJ, Tuch BB, Villén J, Johnson AD, Gygi SP, Morgan DO. Global Analysis of Cdk1
955 Substrate Phosphorylation Sites Provides Insights into Evolution. Science.
956 2009;325(5948):1682–6.
957 23. Huang KL, Chadee AB, Chen CYA, Zhang Y, Shyu AB. Phosphorylation at intrinsically
958 disordered regions of PAM2 motif-containing proteins modulates their interactions with
959 PABPC1 and influences mRNA fate. RNA. 2013;19(3):295–305.
960 24. Dephoure N, Howson RW, Blethrow JD, Shokat KM, O'Shea EK. Combining chemical
961 genetics and proteomics to identify protein kinase substrates. Proc Natl Acad Sci.
962 2005;102(50):17940–5.
963 25. Huang D, Patrick G, Moffat J, Tsai LH, Andrews B. Mammalian Cdk5 is a functional
964 homologue of the budding yeast Pho85 cyclin-dependent protein kinase. Proc National Acad Sci.
965 1999;96(25):14445–50.
966 26. Bett JS, Ibrahim AFM, Garg AK, Kelly V, Pedrioli P, Rocha S, et al. The P-body component
967 USP52/PAN2 is a novel regulator of HIF1A mRNA stability. Biochem J. 2013;451(Pt 2):185–
968 94.
969 27. Hammet A, Pike BL, Heierhorst J. Posttranscriptional regulation of the RAD5 DNA repair
970 gene by the Dun1 kinase and the Pan2-Pan3 poly(A)-nuclease complex contributes to survival of

971 replication blocks. J Biol Chem. 2002;277(25):22469–74.

972 28. Costanzo M, VanderSluis B, Koch EN, Baryshnikova A, Pons C, Tan G, et al. A global

973 genetic interaction network maps a wiring diagram of cellular function. Science.

974 2016;353(6306):aaf1420–aaf1420.

975 29. Lee AY, St.Onge RP, Proctor MJ, Wallace IM, Nile AH, Spagnuolo PA, et al. Mapping the

976 Cellular Response to Small Molecules Using Chemogenomic Fitness Signatures. Science.

977 2014;344(6180):208–11.

978 30. Hoyt MA, Stearns T, Botstein D. Chromosome Instability Mutants of Saccharomyces

979 cerevisiae That Are Defective in Microtubule-Mediated Processes. Mol Cell Biol.

980 1990;10(1):223–34.

981 31. Hoyt MA, Macke JP, Roberts BT, Geiser JR. Saccharomyces cerevisiae PAC2 Functions

982 With CIN1, 2 and 4 in a Pathway Leading to Normal Microtubule Stability. Genetics.

983 1997;146(3):849–57.

984 32. Bhamidipati A, Lewis SA, Cowan NJ. Adp Ribosylation Factor-like Protein 2 (Arl2)

985 Regulates the Interaction of Tubulin-Folding Cofactor D with Native Tubulin. J Cell Biol.

986 2000;149(5):1087–96.

987 33. Geiser JR, Schott EJ, Kingsbury TJ, Cole NB, Totis LJ, Bhattacharyya G, et al.

988 Saccharomyces cerevisiae genes required in the absence of the CIN8-encoded spindle motor act

989 in functionally diverse mitotic pathways. Mol Biol Cell. 1997;8(6):1035–50.

990 34. Amberg DC, Burke DJ, Strathern JN. Inducing yeast cell synchrony: nocodazole arrest. CSH

991 Protoc. 2006;2006(1):pdb.prot4175.

992 35. Schäfer IB, Yamashita M, Schuller JM, Schüssler S, Reichelt P, Strauss M, et al. Molecular

993 Basis for poly(A) RNP Architecture and Recognition by the Pan2-Pan3 Deadenylase. Cell.

994 2019;177(6):1619-1631.e21.

995 36. Tian G, Huang Y, Rommelaere H, Vandekerckhove J, Ampe C, Cowan NJ. Pathway Leading

996 to Correctly Folded β-Tubulin. Cell. 1996;86(2):287–96.

997 37. Siegers K, Waldmann T, Leroux MR, Grein K, Shevchenko A, Schiebel E, et al.

998 Compartmentation of protein folding in vivo: sequestration of non-native polypeptide by the

999 chaperonin–GimC system. EMBO J. 1999;18(1):75–84.

1000 38. Markus SM, Omer S, Baranowski K, Lee W. Improved Plasmids for Fluorescent Protein

1001 Tagging of Microtubules in Saccharomyces cerevisiae. Traffic. 2015;16(7):773–86.

1002 39. Hereford LM, Osley MA, Ludwig JR, McLaughlin CS. Cell-cycle regulation of yeast histone

1003 mRNA. Cell. 1981;24(2):367–75.

1004 40. Fitch I, Dahmann C, Surana U, Amon A, Nasmyth K, Goetsch L, et al. Characterization of

1005 four B-type cyclin genes of the budding yeast Saccharomyces cerevisiae. Mol Biol Cell.

1006 1992;3(7):805–18.

1007 41. Richardson H, Lew DJ, Henze M, Sugimoto K, Reed SI. Cyclin-B homologs in

1008 Saccharomyces cerevisiae function in S phase and in G2. Genes Dev. 1992;6(11):2021–34.

1009 42. Kamiloglu S, Sari G, Ozdal T, Capanoglu E. Guidelines for cell viability assays. Food Front.

1010 2020;1(3):332–49.

1011 43. Xiang K, Bartel DP. The molecular basis of coupling between poly(A)-tail length and

1012 translational efficiency. eLife. 2021;10:e66493.

1013 44. Müller GA, Wintsche A, Stangner K, Prohaska SJ, Stadler PF, Engeland K. The CHR site:

1014 definition and genome-wide identification of a cell cycle transcriptional element. Nucleic Acids

1015 Res. 2014;42(16):10331–50.

1016 45. Stumpf CR, Moreno MV, Olshen AB, Taylor BS, Ruggero D. The Translational Landscape

of the Mammalian Cell Cycle. Mol Cell. 2013;52(4):574–82.

46. Czaplinski K, Singer RH. Pathways for mRNA localization in the cytoplasm. Trends Biochem Sci. 2006;31(12):687–93.

47. Engel KL, Arora A, Goering R, Lo HG, Taliaferro JM. Mechanisms and consequences of subcellular RNA localization across diverse cell types. Traffic. 2020;21(6):404–18.

48. Loedige I, Baranovskii A, Mendonsa S, Dantsuji S, Popitsch N, Breimann L, et al. mRNA stability and m6A are major determinants of subcellular mRNA localization in neurons. Mol Cell. 2023;83(15):2709-2725.e10.

49. Safieddine A, Coleno E, Salloum S, Imbert A, Traboulsi AM, Kwon OS, et al. A choreography of centrosomal mRNAs reveals a conserved localization mechanism involving active polysome transport. Nat Commun. 2021;12(1):1352.

50. Karasu OR, Neuner A, Atorino ES, Pereira G, Schiebel E. The central scaffold protein CEP350 coordinates centriole length, stability, and maturation. J Cell Biol. 2022;221(12):e202203081.

51. Jiang K, Rezabkova L, Hua S, Liu Q, Capitani G, Altelaar AFM, et al. Microtubule minus-end regulation at spindle poles by an ASPM–katanin complex. Nat Cell Biol. 2017;19(5):480–92.

52. Sun M, Jia M, Ren H, Yang B, Chi W, Xin G, et al. NuMA regulates mitotic spindle assembly, structural dynamics and function via phase separation. Nat Commun. 2021;12(1):7157.

53. He Z, Mei L, Connell M, Maxwell CA. Hyaluronan Mediated Motility Receptor (HMMR) Encodes an Evolutionarily Conserved Homeostasis, Mitosis, and Meiosis Regulator Rather than a Hyaluronan Receptor. Cells. 2020;9(4):819.

54. Vineethakumari C, Lüders J. Microtubule Anchoring: Attaching Dynamic Polymers to Cellular Structures. Front Cell Dev Biol. 2022;10:867870.

55. Delgehyr N, Sillibourne J, Bornens M. Microtubule nucleation and anchoring at the centrosome are independent processes linked by ninein function. J Cell Sci. 2005;118(8):1565–75.

56. Panic M, Hata S, Neuner A, Schiebel E. The Centrosomal Linker and Microtubules Provide Dual Levels of Spatial Coordination of Centrosomes. PLoS Genet. 2015;11(5):e1005243.

57. He Z, Wilson A, Rich F, Kenwright D, Stevens A, Low YS, et al. Chromosomal instability and its effect on cell lines. Cancer Rep. 2023;6(6):e1822.

58. Nicholson JM, Macedo JC, Mattingly AJ, Wangsa D, Camps J, Lima V, et al. Chromosome mis-segregation and cytokinesis failure in trisomic human cells. eLife. 2015;4:e05068.

59. Bona MD, Bakhoum SF. Micronuclei and Cancer. Cancer Discov. 2024;14(2):214–26.

60. Cai Y, Hossain MJ, Hériché JK, Politi AZ, Walther N, Koch B, et al. Experimental and computational framework for a dynamic protein atlas of human cell division. Nature. 2018;561(7723):411–5.

61. Sweet TJ, Boyer B, Hu W, Baker KE, Coller J. Microtubule disruption stimulates P-body formation. RNA. 2007;13(4):493–502.

62. Aizer A, Kafri P, Kalo A, Shav-Tal Y. The P Body Protein Dcp1a Is Hyper-phosphorylated during Mitosis. Plos One. 2013;8(1):e49783.

63. Luo Y, Na Z, Slavoff SA. P-Bodies: Composition, Properties, and Functions. Biochemistry. 2018;57(17):2424–31.

64. Sheff MA, Thorn KS. Optimized cassettes for fluorescent protein tagging in Saccharomyces cerevisiae. Yeast. 2004;21(8):661–70.

1063 65. Bähler J, Wu J, Longtine MS, Shah NG, III AM, Steever AB, et al. Heterologous modules
1064 for efficient and versatile PCR-based gene targeting in Schizosaccharomyces pombe. Yeast.
1065 1998;14(10):943–51.
1066 66. Ho CH, Magtanong L, Barker SL, Gresham D, Nishimura S, Natarajan P, et al. A molecular
1067 barcoded yeast ORF library enables mode-of-action analysis of bioactive compounds. Nat
1068 Biotechnol. 2009;27(4):369–77.
1069 67. Douglas AC, Smith AM, Sharifpoor S, Yan Z, Durbic T, Heisler LE, et al. Functional
1070 Analysis With a Barcoder Yeast Gene Overexpression System. G3: GenesGenomesGenet.
1071 2012;2(10):1279–89.
1072 68. Cox JS, Chapman RE, Walter P. The unfolded protein response coordinates the production of
1073 endoplasmic reticulum protein and endoplasmic reticulum membrane. Mol Biol Cell.
1074 1997;8(9):1805–14.
1075 69. Young BP, Loewen CJR. Balony: a software package for analysis of data generated by
1076 synthetic genetic array experiments. BMC Bioinform. 2013;14:354.
1077 70. Tong AHY, Boone C. Yeast Protocol. Methods Mol Biol (Clifton, NJ). 2005;313:171–91.
1078 71. Warde-Farley D, Donaldson SL, Comes O, Zuberi K, Badrawi R, Chao P, et al. The
1079 GeneMANIA prediction server: biological network integration for gene prioritization and
1080 predicting gene function. Nucleic Acids Res. 2010;38(suppl_2):W214–20.
1081 72. Zuberi K, Franz M, Rodriguez H, Montojo J, Lopes CT, Bader GD, et al. GeneMANIA
1082 Prediction Server 2013 Update. Nucleic Acids Res. 2013;41(W1):W115–22.
1083 73. Schindelin J, Arganda-Carreras I, Frise E, Kaynig V, Longair M, Pietzsch T, et al. Fiji: an
1084 open-source platform for biological-image analysis. Nat Methods. 2012;9(7):676–82.
1085 74. Rueden CT, Schindelin J, Hiner MC, DeZonia BE, Walter AE, Arena ET, et al. ImageJ2:

ImageJ for the next generation of scientific image data. BMC Bioinform. 2017;18(1):529.

75. Vuilleumier R, Lian T, Flibotte S, Khan ZN, Fuchs A, Pyrowolakis G, et al. Retrograde BMP signaling activates neuronal gene expression through widespread deployment of a conserved BMP-responsive cis-regulatory activation element. Nucleic Acids Res. 2019;47(2):679–99.

Supporting information captions

SFile 1.docx: Sequence of human PAN2 codon optimized for yeast

SFile 2.xlsx: Synthetic Genetic Analysis (SGA) data for *PAN2* in presence or absence of nocodazole

SFile 3.xlsx: RNA-seq data for *pan2*Δ + WT Pan2 and *pan2*Δ + D1020A Pan2 in presence of nocodazole

SFile 4.avi: Yeast WT with DMSO

SFile 5.avi: Yeast WT with nocodazole

SFile 6.avi: Yeast *pan2*Δ with DMSO

SFile 7.avi: Yeast *pan2*Δ with nocodazole

SFile 8.avi: HEK293 cells - bipolar spindle formation

SFile 9.avi: HEK293 cells - tetrapolar spindle formation